Palaeogeography, Palaeoclimatology, Palaeoecology 625 (2023) 111670

Contents lists available at ScienceDirect

Palaeogeography, Palaeoclimatology, Palaeoecology

journal homepage: www.elsevier.com/locate/palaeo

A 1300-year microfaunal record from the Beaufort Sea shelf indicates exceptional climate-related environmental changes over the last two centuries

Jade Falardeau [a,*], Anne de Vernal [a], Marit-Solveig Seidenkrantz [b], Michael Fritz [c], Thomas M. Cronin [d], Laura Gemery [d], André Rochon [a,e], Vladislav Carnero-Bravo [a,f], Claude Hillaire-Marcel [a], Christof Pearce [b], Philippe Archambault [g]

[a] Geotop Research Center in Earth System Dynamics and Département des sciences de la Terre et de l'atmosphère, Université du Québec à Montréal, C.P. 8888 Succursale Centre-Ville, H3C 3P8 Montréal, Canada
[b] Paleoceanography and Paleoclimate Group, Department of Geoscience, Arctic Research Centre, and iClimate centre, Aarhus University, Høegh-Guldbergs Gade 2, DK-8000 Aarhus C, Denmark
[c] Permafrost Research Unit, Alfred Wegener Institute, Helmholtz Centre for Polar and Marine Research, Telegrafenberg A45, 14473 Potsdam, Germany
[d] U.S. Geological Survey, Florence Bascom Geoscience Center, 12201 Sunrise Valley Drive, National Center, Reston, VA 20192, USA
[e] Institut des sciences de la mer de Rimouski, Université du Québec à Rimouski, 310 allée des Ursulines, G5L 2Z9 Rimouski, Canada
[f] Instituto de Ecología, Universidad del Mar, Campus Puerto Ángel, 70902 Puerto Ángel, Oaxaca, Mexico
[g] Takuvik, Québec Océan, ArcticNet, Département de biologie, Faculté des sciences et de génie, Université Laval, 1045 avenue de la Médecine, G1V 0A6 Québec, Canada

ARTICLE INFO

Editor: Prof. M Elliot

Keywords:
Benthic foraminifera
Ostracods
Tintinnids
Beaufort Sea
Arctic coasts
Climate change

ABSTRACT

The environments of Arctic Ocean nearshore areas experience high intra- and inter-annual variability, making it difficult to evaluate the impact of anthropogenic warming. However, a sediment record from the southern Canadian Beaufort Sea allowed us to reconstruct the impacts of climate and environmental changes over the last 1300 years along the northern Yukon coast, Canada. The coring site (PG2303; 69.513°N, 138.895°W; water depth 32 m) is located in the Herschel Basin, where high sedimentation rates (0.1–0.5 cm a^{-1}) allowed analyses at sub-centennial to decadal resolutions. Benthic foraminiferal, ostracod, and tintinnid assemblages, as well as the stable isotope composition of the foraminifera *Elphidium clavatum* and *Cassidulina reniforme* were used as paleoclimatic and ecological indicators, while the age model was based on the combined radiometric data of ^{14}C, ^{210}Pb and ^{137}Cs. From ca 700 to 1050 CE, our data suggest penetration of offshore shelf-break waters inferred by the dominance of *C. reniforme* followed by the relatively abundant *Triloculina trihedra* in the foraminiferal assemblages as both species are associated with stable saline conditions. Afterwards, the occurrence of ostracods *Kotoracythere arctoborealis* and *Normanicythere leioderma* suggests influx of Pacific-sourced waters until ca. 1150 CE. From ~1150–1650 CE, persistent frigid waters, limited sediment supply, and low abundances of microfossils suggest cold conditions with pervasive annual sea-ice cover that may have restricted upwelling of oceanic waters. After ~1800 CE, the co-occurrence of *Tintinnopsis fimbriata* and bacterial/complex organic carbon feeder foraminifera (*Quinqueloculina stalkeri*, *Textularia earlandi* and *Stetsonia horvathi*), suggest an increased influence of freshwater rich in particulate organic matter, which may be related to the spreading of the Mackenzie River plume and/or increased coastal permafrost erosion during longer ice-free seasons. Based on these proxy data, the shift at ~1800 CE marks the onset of regional warming, which further intensified after ~1955 CE, likely in response to the anthropogenic forcing.

1. Introduction

Sea ice is a key parameter for marine food webs in nearshore Arctic ecosystems, as it influences the timing, flux, and export of primary producers (Grebmeier and Barry, 2007; Nadaï et al., 2021), the upwelling of nutrient-rich subsurface waters onto the continental shelves

* Corresponding author at: Geotop-UQAM, C.P. 8888 Succursale Centre-Ville, H3C 3P8 Montréal, Canada.
E-mail address: Falardeau.jade@courrier.uqam.ca (J. Falardeau).

https://doi.org/10.1016/j.palaeo.2023.111670
Received 8 December 2022; Received in revised form 20 April 2023; Accepted 5 June 2023
Available online 9 June 2023

(Schulze and Pickart, 2012), and vertical mixing and/or stratification (Rainville and Woodgate, 2009; Blais et al., 2017). In the Beaufort Sea, sea-ice cover extent decreased ten times faster from 2000 to 2012 CE (−12.84 days a^{-1}) than during the two previous decades (1979–2000 CE; Frey et al., 2015). The ongoing climate warming likely plays an important role in the decreasing sea-ice cover trend (Notz and Stroeve, 2016), but its temporal and spatial extent also depends on dynamic and thermodynamic factors (Spreen et al., 2011; Frey et al., 2015; Belter et al., 2021). Numerous relationships between the sea-ice cover and large-scale modes of atmospheric circulation, as indicators of dominant wind and thus water mass transport patterns, have been identified (Rigor et al., 2002; Screen and Francis, 2016; Cox et al., 2019; Zhang et al., 2019). These indices may have undergone significant amplitude variations over the last few millennia, notably in relation to the Pacific

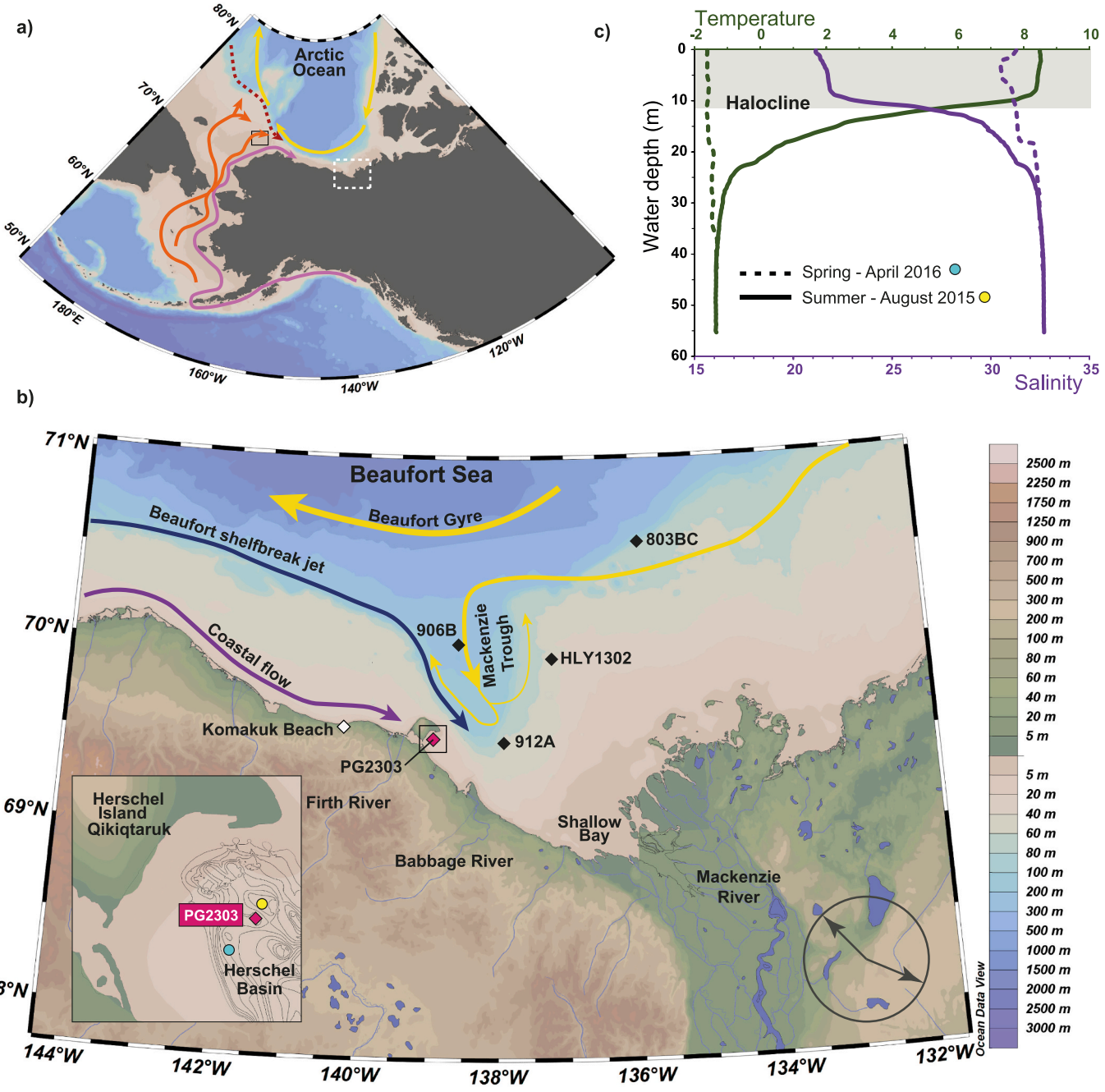

Fig. 1. a) Regional map showing the location of the study area (dotted white square) and the Hanna Shoal (black square). The pink and orange arrows indicate the flow of the Alaskan Coastal Waters (ACW) and other Pacific water branches (winter/summer water masses), respectively; the dotted red arrow shows the path of the subsurface Atlantic Water along the continental margin, and the yellow arrows represent the Beaufort Gyre based on Grebmeier et al. (2006). b) Map of the study area showing the coastal flow (purple arrow), the Beaufort shelfbreak jet (dark blue arrow), and the waters recirculating in the Mackenzie Trough under the Beaufort Gyre influence (yellow arrows) based on Lin et al. (2020). The gray arrows in the lower right corner mark the dominant wind directions (Radosavljevic et al., 2016), the black diamonds show the location of cores mentioned in the text, and the white diamond shows the location of the Komakuk Beach weather station. In the lower-left corner is a close-up of the study area with the core site location (pink diamond) and bathymetry of the Herschel Basin (EBA Engineering Consultants Ltd., 1992). c) Salinity (purple) and temperature (green) profiles in the Herschel Basin in August 2015 (solid line) and April 2016 (dotted lines) from CTD data (Falardeau et al., 2023). The blue and yellow dots refer to the location of the CTD measurements shown in the close-up of Fig. 1b, while the gray shading area separates the local surface waters from the bottom waters. (For interpretation of the references to colour in this figure legend, the reader is referred to the web version of this article.)

Decadal Oscillation (PDO; Mantua and Hare, 2002) and the Arctic Oscillation (AO; Thompson and Wallace, 1998) as suggested by terrestrial and marine proxies (MacDonald and Case, 2005; Darby et al., 2012; Lapointe et al., 2017).

For a complete understanding of climate dynamics in the past, long time series are needed to assess the interplay between different environmental forcings, including their relationships to sea-ice cover and, thus, how they influence oceanic conditions and productivity. Furthermore, these time series help identify natural variability, which in turn can serve to sort out the effects and the magnitude of recent anthropogenic climate changes. To a certain extent, reconstructions of past conditions in the nearshore environments could also offer insights into marine biological resources and their tolerance to changes over centuries of harvesting, i.e. fisheries, in the Beaufort Sea (Usher, 2002; Friesen et al., 2020). Over the last two millennia, large-amplitude climatic events have been inferred in the terrestrial environment of northwestern America based on tree rings and sediment cores in lakes (e.g. Rühland et al., 2003; Bird et al., 2009; Viau and Gajewski, 2009; Fritz et al., 2012; Anchukaitis et al., 2013; Porter et al., 2013; Wolter et al., 2017; Nicolle et al., 2018) and in offshore marine environments of the Beaufort Sea (Richerol et al., 2008; Schell et al., 2008; Bringué and Rochon, 2012; Scott et al., 2009; Kutos et al., 2021). However, Canadian Beaufort Sea continental shelf records are rare (Seidenstein et al., 2018; Gemery et al., 2023), especially near the coasts.

The first objective of this study is to reconstruct the environmental conditions of the Canadian Beaufort Sea shelf over the last millennium, where harvesting of marine biological resources has been and still is extremely important for local communities. Our study's second objective is to disentangle the effect of anthropogenic activities from the natural variability. To meet these objectives, we document past marine conditions, focusing on evaluating changes in sea ice, water temperature and salinity, as well as marine productivity. We base the study on microfossil investigations of two marine sediment cores retrieved at the same site (PG2303) in the Herschel Basin, northern Yukon, Canada. The study site is in an area of relatively high and continuous sediment accumulation, which enables sub-decadal temporal resolution over millennia (Grotheer et al., 2020), together with abundant, diverse, and well-preserved microfossils (Falardeau et al., 2023).

2. Regional setting

Coring site PG2303 is in the Herschel Basin on the continental shelf off northern Canada (Fig. 1a, b). The basin is located 3 km west of Herschel Island-Qikiqtaruk, and 7 km north of the Yukon coast (Fig. 1b). The organic carbon sequestered in Herschel Basin is dominated by terrestrial sources. It is derived either from coastal erosion of Herschel Island-Qikiqtaruk and the mainland coast or from particulate matter transported by the Mackenzie River (Grotheer et al., 2020), with the Mackenzie River mouth located at Shallow Bay ca 130 km east of our study site (Fig. 1b). Today, suspended particulate matter from the Mackenzie River reaches the study site during the spring freshet when turbidity is at a maximum (Juhls, 2021) and under easterly winds (Wood et al., 2015). The spring freshet occurs from mid-May to the end of June (Carmack and Macdonald, 2002; Mulligan and Perrie, 2019). On average, the sea ice break-up occurs by the end of June, and sea ice forms again around mid-October (Carmack and Macdonald, 2002; Frey et al., 2015).

Hydrographic conditions in the area depend on local winds. Generally, the Beaufort shelfbreak jet flows eastward, transporting cold and saline nutrient-rich Pacific winter waters (blue arrow; Fig. 1b; Pickart, 2004; hereafter referred to as Pacific waters). They are also known as the Remnant Winter Water (Lin et al., 2020). These Pacific waters overlay the dense, warm, and saline Atlantic waters (dotted red arrow; Fig. 1a; Lin et al., 2020). Alongshore, the coastal flow transports warmed meteoric waters or sea-ice meltwaters and possibly warmer and less saline Pacific summer waters towards the east (purple arrow; Fig. 1b; Lin et al., 2020). Offshore, the Beaufort Gyre circulates clockwise, causing recirculation in the Mackenzie Trough (yellow arrows; Fig. 1a, b; Lin et al., 2020). Dominant winds are either from the northwest or the east-south-east (Fig. 1b; Radosavljevic et al., 2016). Easterly wind events favor the upwelling of shelf-break waters onto the continental shelf, decreased sea-ice cover, and enhanced primary productivity (Tremblay et al., 2011, 2012; Pickart et al., 2013). In contrast, westerly winds are unfavorable for upwelling and lead to persistent sea-ice cover (Carmack and Macdonald, 2002; Pickart et al., 2011). The water column in the Herschel Basin is stratified in summer with a freshwater layer 7–15 m thick at the surface above the frigid (<0 °C) and saline waters at the bottom (Fig. 1c; Mulligan et al., 2010). The Herschel Basin bottom waters are formed by a mixture of brines from sea-ice formation in winter and upwelled waters from the shelf break (Williams and Carmack, 2012).

3. Methods

3.1. Sediment cores

Marine sediment core PG2303 was collected with a UWITEC piston corer on April 20th, 2016, using a tripod placed on the sea ice, as part of the Yukon Coast spring expedition led by the Alfred Wegener Institute in Potsdam, Germany (Fig. S1). The 12.3 m long core was collected in 32 m water depth at 69.513°N and 138.895°W in clastic mud (Falardeau et al., 2023). The sediment record is constructed as a composite sequence of five overlapping core segments that were correlated based on magnetic susceptibility (Pfalz, 2017). It covers about 4000 years of sedimentation (Grotheer et al., 2020). In this study, we focus on the upper 322 cm of the core, which encompasses the last 1300 years (see Section 4.1; Fig. 2; Table S1). The core was subsampled at 10-cm intervals from 322 to 62 cm and at 5-cm intervals from 62 cm to the top of the core (Table S2); subsamples were 1-cm thick.

During the same expedition, a short surface sediment core of 20 cm in length (PG2303–1) was collected at the same site using a UWITEC gravity corer to recover the water-sediment interface better. It was stored cool before subsampling at 1-cm intervals using a vertical extruder. The short core likely covers the last two decades (see Section 4.1; Fig. S2; Appendix A; Falardeau et al., 2023).

3.2. Grain size

A minimum of 0.2 g of dry sediment per sample was weighed for grain size analysis. Next, the sediment was mixed with hydrogen peroxide (30%) to remove organic matter. Once the reaction was complete, the samples were measured in the Microtrac MRB Bluewave laser diffraction instrument at the Geotop-UQAM. The instrument can detect grain sizes from 0.01 to 2000 μm. The data were processed in GRADISTAT (Blott, 2010), which defines sand as particles between 2 mm and 63 μm, silt between 63 and 2 μm, and clays <2 μm. Results are reported in Table S3.

3.3. Radiometric chronology

The age models were defined based on radiometric analyses, combining ^{210}Pb, ^{226}Ra, ^{137}Cs and ^{14}C measurements; fore core PG2303 all methods were used, while for PG2303–1 we concentrated on ^{210}Pb, ^{226}Ra, and ^{137}Cs. The age model for PG2303–1 has previously been presented by Falardeau et al. (2023), who showed that the bottom of this core may be dated to 1999 ± 6 CE.

For core PG2303, fifteen samples in the upper 75 cm of the core were analyzed for ^{210}Pb, ^{226}Ra and ^{137}Cs at Geotop-UQAM (Table S2). For ^{210}Pb, a spike of ^{209}Po was added into the ground sediment samples (~1 g), before it was successively digested in three different acids (HNO_3; HCl, HF and HNO_3), and in hydrogen peroxide with acid (H_2O_2 and HNO_3). Then, the residue was dissolved in HCl 0.5 N with ascorbic acid.

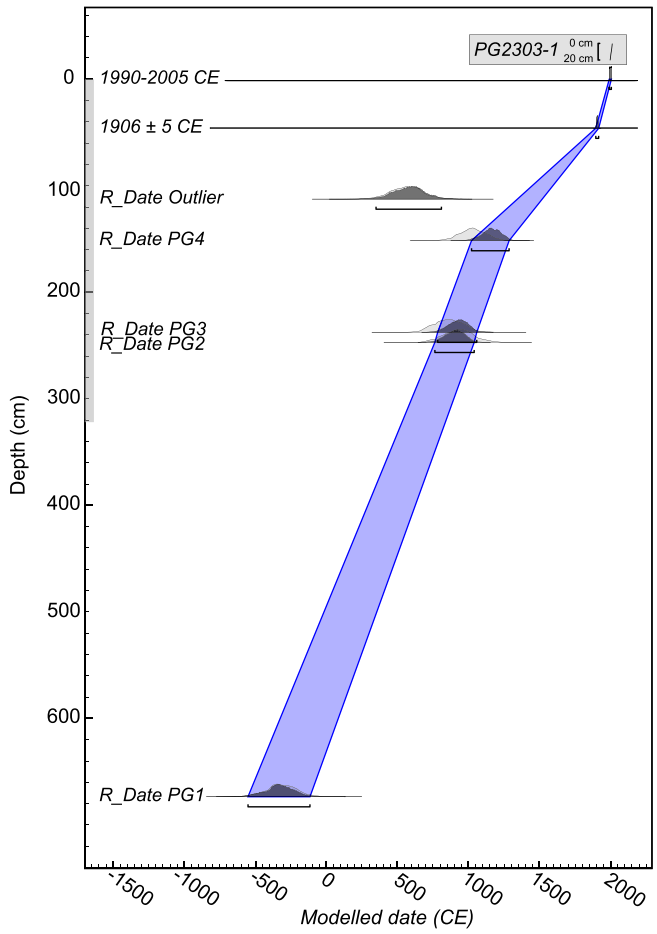

Fig. 2. Core PG2303 age model based on *OxCal* (version 4.4; Bronk Ramsey, 2008, 2009). The vertical gray bar indicates the length of the core section used for this study. The blue shading indicates the 2-sigma probability range of the age depth model. Details on the two constrained ages based on ^{210}Pb and ^{137}Cs activity profiles at the top of the core can be found in the methods Section 3.3 and Appendix A. The age model of core PG2303–1 (20–0 cm) from Falardeau et al. (2023) is illustrated in the gray rectangle in the top right corner. (For interpretation of the references to colour in this figure legend, the reader is referred to the web version of this article.)

The ^{209}Po (recovery of the internal tracer) and the ^{210}Po activities (sample) were measured by alpha spectrometry using ORTEC detectors coupled to Maestro™ data acquisition software on silver disks. We calculated ^{210}Pb by assuming secular equilibrium between ^{210}Pb and ^{210}Po. The ^{226}Ra and ^{137}Cs were measured using high-resolution gamma spectrometry with a germanium detector (ORTEC). Samples were dried and sealed in plastic containers for at least 3 weeks prior to measurement. The ^{226}Ra activity average can represent the value of supported lead ($^{210}Pb_{sup}$) in the core. The excess of ^{210}Pb ($^{210}Pb_{ex}$) is obtained by subtracting the $^{210}Pb_{sup}$ from the total activity of ^{210}Pb ($^{210}Pb_{tot}$).

Four ^{14}C ages on biogenic carbonates, i.e.mollusk shells and large specimens of the benthic foraminifera *Vaginulina* sp., measured at the AMS facility at the University of Cologne and the Alfred Wegener Institute (AWI) MICADAS laboratory were used to constrain the age model of core PG2303 (Table 1). The two ^{14}C ages at 248–246 cm and 238–237 cm delivered similar ages ranging ~861–932 CE (Table 1), offering a robust age anchor at this core depth interval. The model was constructed using the *OxCal* program (version 4.4; Bronk Ramsey, 2008, 2009) and we applied the Marine20 curve (Heaton et al., 2020). We used a ΔR of 330 ± 41 years based on a 3600-year-old tephra layer in a sediment core of the Chukchi Sea (Pearce et al., 2017; West et al., 2022). It is similar to the ΔR of 308 ± 111 years based on ^{14}C ages of seven mollusks collected in the nearshore areas of Alaska prior to bomb testing (Table S4; cf. McNeely et al., 2006). These two independent ΔR suggest that the reservoir effect in the area was most probably constant over the last few millennia.

While the overall age model of PG2303 is based on radiocarbon dating, the radiogenic isotope activity of ^{210}Pb, ^{226}Ra, and ^{137}Cs in the top 75 cm helped constrain the upper part of the age model. We used the core depth at which the supported ^{210}Pb is reached, i.e. 1906 CE at 46 ± 2 cm (Fig. S2), as an age marker (Fig. 2). Moreover, we assumed that the drop in ^{137}Cs recorded at 14.5–9.5 cm core depth (midpoint at 12 cm; Fig. S2) correlated to the drop in atmospheric ^{137}Cs fallout at ~1980 CE (Kuzyk et al., 2013). As the tintinnid concentrations and grain size data between the top of core PG2303 and the bottom of core PG2303–1 show no communalities (Fig. 3), we interpret the top of core PG2303 to be older than the age at the bottom of core PG2303–1 and that there is no overlap between the cores. Thus, the top of core PG2303 must be older than 1999 ± 6 CE (cf. Falardeau et al., 2023). Nevertheless, the total inventory of ^{137}Cs in PG2303 indicates that only a limited amount of surface sediment has been lost in the coring process (cf. Kuzyk et al., 2013). Using levels for the drop in ^{137}Cs and for the supported ^{210}Pb, we calculated a mean sedimentation rate of 0.44 ± 0.06 cm a^{-1} for this interval and extrapolated the age upwards. This gave an age of 2010 ± 20 CE for the core top, but due to the maximal possible age of 1999 ± 6 CE at the core top, we reduced the possible range to 1990–2005 CE (Fig. 2; see Fig. S2 and Appendix A for more details).

The sediment mass accumulation (g $cm^{-2}a^{-1}$) results from the calculated mean sedimentation rates (cm a^{-1}) based on the *OxCal* age model multiplied by the mean density of 1.05 ± 0.05 g cm^{-3}. The mean density was calculated from the fifteen samples measured for ^{210}Pb,

Table 1
^{14}C ages on core PG2303 calibrated according to Marine20 with the CALIB 8.20 calibration program (Stuiver and Reimer, 1993) in consideration of a ΔR of 330 ± 41 years. The ^{14}C age in gray was not considered in the model. The ^{14}C ages with a laboratory sample ID starting with AWI and COL were measured at AWI MICADAS and at the University of Cologne, respectively.

Date name as reported in Fig. 2	Depth (cm)	Uncalibrated ^{14}C age (years BP)	Calibrated age range (2 sigma) (cal. years BP)	Median age (cal. years BP)	Median age (years CE)	Dated material	Reference	Laboratory sample ID
Outlier	112–113	2313 ± 80	1164–1618	1385	565	One large specimen of benthic foraminifer *Vaginulina* sp.	This study	AWI-7126.1.1
PG4	151–152	1865 ± 41	738–1099	921	1029	Bivalve; *Nuculana* sp.	Grotheer et al. (2020)	COL4367.1.1
PG3	237–238	2024 ± 67	898–1283	1089	861	One large specimen of benthic foraminifer *Vaginulina* sp.	This study	AWI-7127.1.1
PG2	246.5–247.5	1955 ± 65	813–1231	1018	932	Mollusk	This study	AWI-7148.1.1
PG1	673.5	3062 ± 47	2050–2492	2269	−319	Bivalve; *Nuculana* sp.	Grotheer et al. (2020)	COL4368.1.1

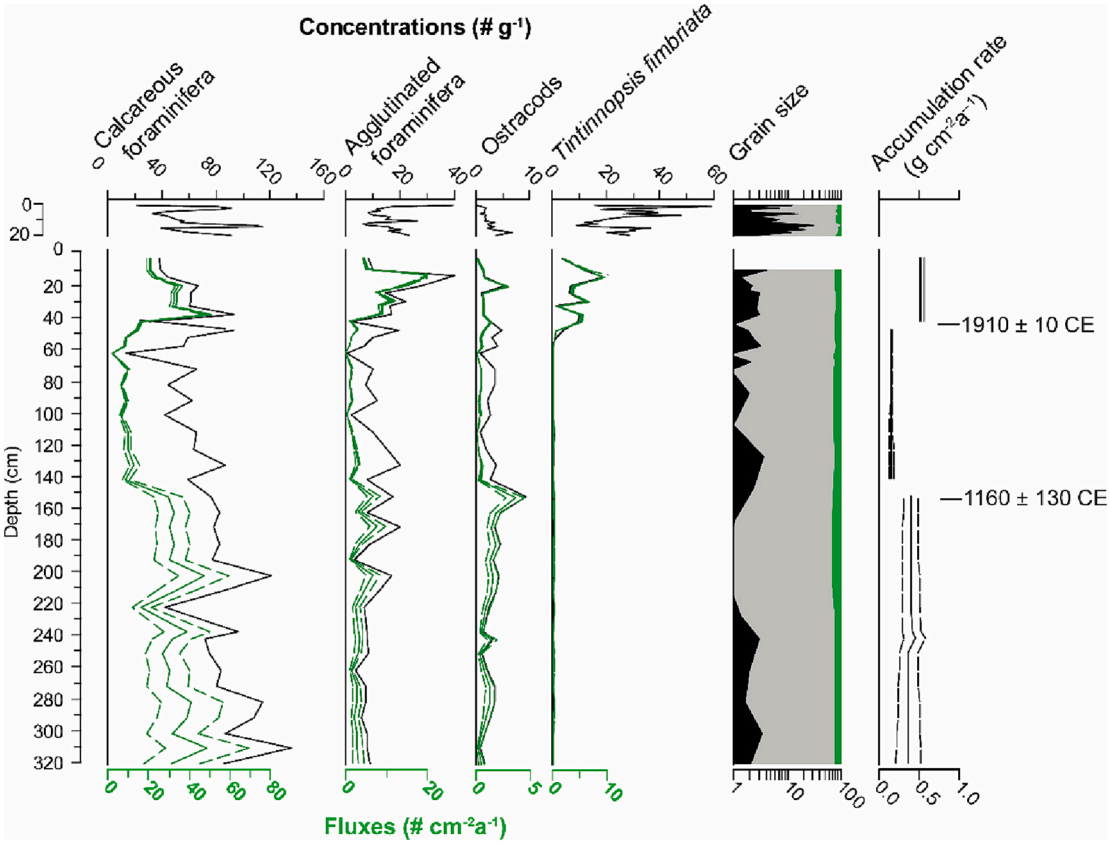

Fig. 3. Microfossil concentrations (black lines), fluxes (green lines), grain size (black = sand; gray = silt; green = clay), and mass accumulation rates of the composite sequence of cores PG2303–1/PG2303 as a function of depth (cm). Dashed lines represent the flux and mass accumulation rate errors. (For interpretation of the references to colour in this figure legend, the reader is referred to the web version of this article.)

which showed homogeneous values (Table S5). Uncertainties on the accumulation rates follow the propagation of the errors on the ages and the density.

3.4. Micropaleontological preparations

A total of 39 subsamples (~6 g of dried sediment) from core PG2303 were dried, weighed, and subsequently wet sieved at 63 μm. The >63 μm fraction was used to observe and count microfossils under a binocular microscope at 40×. In three samples, fine sand was abundant, and we used dense liquid (tetrachlorethylene, C_2Cl_4) to separate mineral grains from biogenic remains (Table S2). The most common microfossils were benthic foraminifera, ostracods, and tintinnids.

The identification of foraminifera largely follows previous work by Feyling-Hanssen et al. (1971), Polyak et al. (2002), Scott et al. (2008a), and Jennings et al. (2020). All benthic foraminiferal taxa identified in this study are the same as those found in the short core PG2303–1 collected at the same site in the Herschel Basin (Table 2a). For a detailed description of the micropaleontological content in the gravity core PG2303–1, see Falardeau et al. (2023). All calcareous benthic foraminiferal taxa belonging to the Polymorphinoidea superfamily were grouped as "polymorphinids" (Table S6).

For the ostracod community, some taxa occurred exclusively in core PG2303. Among these, *Acanthocythereis dunelmensis*, *Roundstonia globulifera*, *Cytheropteron biconvexa*, *Kotoracythere arctoborealis* and *Normanicythere leioderma* are reported here for the first time in the Herschel Basin (Table 2b). Their identification is based on Gemery et al. (2017) and Stepanova et al. (2003). The ostracods are categorized into two groups following their tolerance to salinity (Table 2b); the low salinity tolerant (LST) taxa and the euhaline taxa, which prefer salinity >30 psu.

The only reported species of tintinnids in cores PG2303 and PG2303–1 is *Tintinnopsis fimbriata* (Meunier, 1919; Agatha, 2008). *T. fimbriata* is an agglutinated ciliate that uses small mineral particles to build its shell (lorica). It was reported as *Tintinnopsis rioplatensis* (Souto, 1973) in Scott et al. (2008a).

We calculated the concentrations (# g^{-1} sediment) of calcareous benthic foraminifera, agglutinated benthic foraminifera, ostracods, and *T. fimbriata* by dividing the total counts by the dry mass in each sample. For microfossil fluxes (# $cm^{-2}a^{-1}$), we multiplied the concentrations (# g^{-1}) with the accumulation rates (g $cm^{-2}a^{-1}$). We considered the uncertainties in accumulation rates to calculate the errors in the fluxes. Next, we calculated the relative abundance (%) of benthic foraminiferal and ostracod taxa. The benthic foraminiferal counts are reported as the relative frequency of the taxa versus the total benthic foraminiferal (calcareous and agglutinated) assemblage. The agglutinated foraminifera are found in lower numbers, but we also calculated the percentage of the calcareous and agglutinated species separately, together with the total foraminiferal concentrations and fluxes (Fig. S3). Finally, we used the Arctic Ostracode Database 2020 (AOD2020; Cronin et al., 2021) and built distribution maps of selected species using Ocean Data View (Schlitzer, 2018; Fig. S4).

The percentages of foraminifera are considered statistically significant for dominant taxa (>5%) when a minimum of 100 foraminiferal tests are counted per sample, although >300 specimens should normally be counted to fully account for the proportions of rare species (Fatela and Taborda, 2002). For ostracods, we considered abundances of ≥10 valves as significant. All counts of calcareous benthic foraminifera satisfied the minimum threshold value of 100 with a mean of 458 ± 173 specimens per sample, with one exception (sample at 63–62 cm; 1790 ± 30 CE; 78 foraminifera counted; Table S6). When calcareous and agglutinated foraminiferal specimens are combined, counts <300 are reached in only seven samples, among those two have a sum <200.

Table 2a
List of benthic foraminiferal and tintinnid taxa identified in the cores (x = present).

	PG2303	PG2303–1
Calcareous foraminifera		
Bolivinellina pseudopunctata (Höglund, 1947)	x	x
Buccella frigida (Cushman, 1922)	x	x
Cassidulina reniforme Nørvang, 1945	x	x
Cornuspira involvens (Reuss, 1850)	x	x
Elphidiella groenlandica (Cushman, 1933)	x	–
Elphidium albiumbilicatum (Weiss, 1954)	x	x
Elphidium asklundi Brotzen, 1943	x	x
Elphidium bartletti Cushman, 1933	x	x
Elphidium clavatum Cushman, 1930	x	x
Elphidium hallandense Brotzen, 1943	x	x
Eoeponidella pulchella (Parker, 1952a)	x	x
Epistominella takayanagii Iwasa, 1955	x	x
Haynesina nivea (Lafrenz, 1963)	x	x
Haynesina orbicularis (Brady, 1881a)	x	x
Islandiella helenae Feyling-Hanssen & Buzas, 1976	x	x
Islandiella norcrossi (Cushman, 1933)	x	x
Nonionellina labradorica (Dawson, 1860)	x	x
Polymorphinoidea	x	x
Pyrgo williamsoni (Sylvestri, 1923)	x	x
Quinqueloculina stalkeri Loeblich & Tappan, 1953	x	x
Quinqueloculina seminulum (Linnaeus, 1758)	x	x
Stainforthia feylingi Knudsen & Seidenkrantz, 1994	x	x
Stainforthia loeblichi (Feyling-Hanssen, 1954)	x	x
Stetsonia horvathi Green, 1960	x	x
Triloculina trihedra Loeblich & Tappan, 1953	x	x
Vaginulina trondheimensis (Feyling-Hanssen, 1964)	x	–
Valvulineria spp. Cushman (1926)	x	x
Agglutinated foraminifera		
Ammotium cassis (Parker, 1870)	–	x
Cribrostomoides crassimargo (Norman, 1892)	x	x
Eggerelloides advenus (Cushman, 1922)	x	x
Lagenammina difflugiformis (Brady, 1876)	x	x
Portatrochammina karica Shchedrina, 1946	x	x
Recurvoides turbinatus (Brady, 1881b)	x	x
Spiroplectammina biformis (Parker & Jones, 1865)	x	x
Textularia earlandi Parker, 1952b	x	x
Textularia torquata Parker, 1952a	x	x
Tintinnids		
*Tintinnopsis fimbriata*Meunier, 1919	x	x

Thus, we are confident in the robustness of the foraminiferal assemblage data. Ostracod valve counts ranged from one to 45 with a mean of 15 ± 11 valves per sample (Table S6). We calculated the percentages of ostracod taxa for all samples, but assemblages should be considered with caution especially with low abundance counts of <10 valves. For *T. fimbriata*, there were <10 loricae counted per sample below 53 cm, but the counts reached a mean of 53 ± 31 specimens in the upper part of the core. Only the concentrations and fluxes are presented for the tintinnids as one species was identified.

3.5. PCA analyses and community diversity

We performed a principal component analysis (PCA) to guide the identification of significant shifts and to divide the record of benthic foraminiferal and ostracod assemblages in the composite sequence of cores PG2303–1 and PG2303 into ecozones. For the abundant and diverse benthic foraminiferal assemblages (calcareous and agglutinated taxa included), we included taxa that occurred in at least 20 out of the 74 samples of the composite core and that were ≥ 2% of the assemblages in at least one sample. Then, we analyzed the samples with ≥300 test counts. For ostracods, all taxa were kept, but we ran the analysis only on samples with counts of 10 valves or more. For the PCA, we used the vegan package (Oksanen et al., 2013) on the standardized (z-scores) relative abundances using the R software (R Core Team, 2021).

The Shannon diversity index (Shannon, 1948) was used as an indicator of diversity, which is the exponential of the Shannon entropy. The Shannon diversity index was calculated on the *Hellinger*-transformed raw counts of foraminifera and ostracods of the composite core in the vegan package under R. For foraminifera, the specimens identified to the genus level were discarded, except those belonging to specimens usually identified at the genus level, such as *Valvulineria* spp. (see Table 2a). We calculated the Shannon diversity index at the genus level for the ostracods.

3.6. Stable isotopes

The isotopic composition ($\delta^{18}O$ and $\delta^{13}C$ ‰ vs. VPDB) of benthic foraminiferal tests was measured on *Elphidium clavatum* and *Cassidulina reniforme*. For each species, between 50 and 120 μg from the >63 μm fraction (equivalent to about 80–200 specimens of *E. clavatum* and

Table 2b
List of ostracod taxa identified in the cores (x = present).

	PG2303	PG2303–1	Low Salinity Tolerant	Euhaline	References
Acanthocythereis dunelmensis (Norman, 1869)	x	–	x		5
Cluthia cluthae (Brady, Crosskey & Robertson, 1874)	x	–		x	1, 5, 6
Cytheropteron biconvexa Whatley and Masson,1979	x	–		x	1, 3
Cytheropteron brastadensis Lord, 1981/*Cytheropteron discoveria* Brouwers, 1994	x	x		x	1, 2, 6
Cytheropteron elaeni Cronin, 1989	x	x		x	2, 4, 5
Cytheropteron sulense Lev, 1972	x	x		x	5
Cytheropteron suzdalskyi Lev, 1972	x	x		x	2
Eucythere spp.: *Eucythere argus* (Sars, 1866); *Eucythere declivis* (Norman, 1865)	x	x	x		5
Eucytherura delineata Whatley & Eynon, 1996	x	x		x	4
Heterocyprideis sorbyana (Jones, 1857)	x	x	x		3, 5, 6
Kotoracythere arctoborealis Schornikov & Zenina, 2006	x	–		x	7
Loxoconcha venepidermoidea (Swain, 1963)	x	x	x		2
Normanicythere leioderma (Norman, 1869)	x	–		x	1, 2, 5
Paracyprideis pseudopunctillata Swain, 1963	x	x	x		2, 3, 4, 5
Rabilimis mirabilis (Brady, 1868)	x	x		x	1, 2, 5
Roundstonia globulifera (Brady, 1868)	x	–	x		5
Semicytherura complanata (Brady, Crosskey & Robertson, 1874)	x	x		x	6

1- Olausson (1982).
2- McDougall et al. (1986).
3- Stepanova et al. (2003).
4- Gemery et al. (2017).
5- Stepanova et al. (2019).
6- Tian et al. (2020).
7- Gemery et al. (2021).

60–150 specimens of *C. reniforme*) were weighed with a microbalance and transferred into conical glass vials. The vials were closed with septum caps and heated at 90° for an hour prior to the analysis at Geotop-UQAM. The laboratory uses a Micromass Isoprime isotope ratio mass spectrometer coupled to a MultiCarb system in dual inlet mode. In some intervals, successive samples were grouped to reach a suitable mass of calcium carbonate. Some samples could not be measured due to insufficient mass (Table S7). The results were normalized using two internal reference materials ($\delta^{18}O = -1.48 \pm 0.03$ ‰ and -14.25 ± 0.05 ‰; $\delta^{13}C = 2.21 \pm 0.03$‰ and -40.78 ± 0.05‰). The analytical uncertainty is less than ±0.05 ‰ and ± 0.08 ‰ for $\delta^{18}O$ and $\delta^{13}C$, respectively.

E. clavatum tests have shown a disequilibrium of around −0.6 to −1.0 ‰ vs. VPDB (Erlenkeuser and von Grafenstein, 1999; Polyak et al., 2003), but also a positive one of +1.0 ‰ vs. VPDB (Bauch et al., 2004), for $\delta^{18}O$ in other studies of Arctic sediments. *E. clavatum* is known to have different offsets depending on water salinity (Polyak et al., 2003; Bauch et al., 2004). Therefore, although it is one of the most common species on Arctic Ocean shelves, *E. clavatum* is not ideal for isotopic analysis in shallow estuarine environments. Nevertheless, since the studied core site is from the deeper part of the basin, below the pycnocline (Fig. 1c), the isotope data should reflect a relatively stable and saline environment. *C. reniforme* normally calcifies close to equilibrium with a low vital offset of 0.13 ± 0.2 ‰ (Austin and Kroon, 1996).

Negative $\delta^{13}C$ values of *E. clavatum* have been reported in previous studies (Erlenkeuser and von Grafenstein, 1999; Polyak et al., 2003; Bauch et al., 2004), which would suggest infaunal habitats where pore waters are depleted in ^{13}C (McCorkle et al., 1990). Indeed, *E. clavatum* often lives as shallow infaunals in the upper millimeters of sediment (Murray, 2006) and can tolerate high sedimentation rates and burial (Ullrich et al., 2009), while *Cassidulina* can be both epifaunal and infaunal (Murray, 2006).

Seawater samples were poured from a water sampler at the sampling site directly into 30 mL narrowneck LDPE bottles. Samples were stored dark and cool at +4 °C prior to analysis. The oxygen ($\delta^{18}O$) and hydrogen ($\delta^{2}H$) stable isotope compositions of precipitation were measured in the Stable Isotope Facility of the Alfred Wegener Institute in Potsdam (Germany), using a Finnigan MAT Delta-S mass spectrometer ($1\sigma < 0.1$ ‰ for $\delta^{18}O$, $1\sigma < 0.8$ ‰ for $\delta^{2}H$; Meyer et al., 2000). Values are given as per mil (‰) difference from the Vienna Standard Mean Ocean Water (VSMOW) standard (see data in Table S8). The $\delta^{18}O$ in the water was used to calculate the equilibrium calcite $\delta^{18}O$ as a function of salinity using the equation of Shackleton (1974) modified for the PDB scale (Hut, 1987) based on Polyak et al. (2003) and assuming stable water temperatures of −1 °C (Fig. 1c). The equation is:

$$\text{Equilibrium calcite } \delta^{18}O = \delta^{18} \times O_{\text{water}} - 0.27 + (\text{Temperature } [^{\circ}C] - 16.9)/-4.0$$

4. Results

4.1. PG2303 grain size and age model

The ratios between sand, silt, and clay are relatively constant throughout core PG2303, with concentrations ranging from 1 to 4%, 63–74%, and 23–36%, respectively. The *OxCal* model performed on the ^{14}C data for core PG2303 yielded ages of 690 ± 150 CE in the bottom sample (322–321 cm) up to 1998 ± 8 CE at core top (Fig. 2). The mean mass accumulation rates are 0.38 ± 0.02 g cm^{-2} a^{-1} from the bottom to 1160 ± 130 CE, then they decrease to 0.15 g cm^{-2} a^{-1}, subsequently again increasing to 0.52 g cm^{-2} a^{-1} from 1910 ± 10 CE to the core top (Fig. 3). The bottom of the short core PG2303–1 is younger than the top of the long piston core PG2303 in accord with high $^{210}Pb_{tot}$ values and sedimentological and micropaleontological data (see Section 3.3; Fig. S2; Appendix A; Falardeau et al., 2023).

4.2. PG2303 Microfossil abundances

The most abundant microfossils reported in this study are calcareous benthic foraminifera with mean concentrations of 72 ± 25 g^{-1}. The concentrations decrease by half towards the core top, with values of ~106 g^{-1} at the bottom of the core (690 ± 150 CE) down to mean values of 55 ± 20 g^{-1} at <110 cm (>1440 ± 90 CE; Fig. 3). The flux of calcareous foraminifera is estimated at 25 ± 13 cm^{-2}a^{-1}, with recurrent higher values prior to 1160 ± 130 CE (mean of 33 ± 7 cm^{-2} a^{-1}).

The concentrations of agglutinated benthic foraminifera average 11 ± 8 g^{-1} and their fluxes average 4 ± 4 cm^{-2} a^{-1}. A distinct interval of low agglutinated foraminiferal abundances occurs around 120–50 cm (~1330–1880 CE) with mean concentrations of 7 ± 4 g^{-1} and mean fluxes of 1 ± 1 cm^{-2} a^{-1}. However, the presence of calcareous and agglutinated foraminifera throughout the record suggests good preservation.

The concentration of ostracods ranges from 1 to 6 valves g^{-1}, except for a maximum of 9 valves g^{-1} at 1160 ± 130 CE (Fig. 3), corresponding to a maximum flux of 4 ± 1 valves cm^{-2} a^{-1}. *Tintinnopsis fimbriata* abundance is low until 53 cm (1825 ± 20 CE; <1 g^{-1}). Afterward, mean *T. fimbriata* concentrations are 8 ± 5 g^{-1} and fluxes are 4 ± 3 cm^{-2} a^{-1}.

4.3. Benthic foraminiferal assemblages

A total of 22 species of calcareous and 11 species of agglutinated benthic foraminiferal taxa were identified (Table 2a). There was no indication of dissolution of the carbonate tests. The Shannon diversity index is 12 ± 2 in cores PG2303–1/PG2303 but reaches recurrent lower values towards the present (<10; Fig. 4). *Elphidium clavatum* and *Cassidulina reniforme* dominate the assemblages of core PG2303 with percentages of 35 ± 7% and 24 ± 8% of the calcareous and agglutinated assemblage, respectively. *Spiroplectammina biformis* is the dominant agglutinated taxa with relative abundances ranging from 5 to 35%. *Islandiella helenae*, *Haynesina orbicularis*, *Haynesina nivea, Buccella frigida*, *Eoeponidella pulchella*, *Stainforthia feylingi*, polymorphinids, and *Textularia torquata* are occasional accompanying taxa (0–10%). *Islandiella norcrossi*, *Elphidium asklundi*, *Epistominella takayanagii*, *Quinqueloculina stalkeri*, *Triloculina trihedra, Stetsonia horvathi*, *Textularia earlandi*, and *Recurvoides turbinatus* are common, but occur in low percentages (<3%; Fig. 4; Table S6). *Stainforthia loeblichi* and *Bolivinellina pseudopunctata* were also recovered in addition to rare specimens of *Cornuspira* spp., *Elphidium bartletti* and the agglutinated *Cribrostomoides crassimargo*, *Portrochammina karica* and *Eggerelloides advenus* (Tables 2a and S6).

The PCA of benthic foraminiferal assemblages revealed that the first principal component (PC1) explains 28% of the variance (Fig. 5; See Table 3 for the corresponding abbreviation names). Negative PC1 scores characterize the modern assemblages (samples younger than 1790 ± 30 CE; Fig. 5), which are marked by the increase of *T. earlandi*, *S. feylingi*, *E. pulchella*, *H. nivea*, *S. horvathi*, *S. biformis*, and *Q. stalkeri* (Figs. 4-5). The second principal component (PC2) explains 15% of the variance. It shows an opposition between the agglutinated taxa *R. turbinatus*, *S. biformis* and *T. torquata* together with the calcareous taxon *B. pseudopunctata* against *H. nivea*, *E. clavatum*, *E. pulchella*, and *B. frigida* (Fig. 5).

The foraminiferal assemblages were divided into three ecozones based on the PCA results. Ecozone F-III is distinguished by positive PC2 values from 690 ± 150 to 950 ± 140 CE (Figs. 4-5). However, Ecozone F-III, is more importantly defined by the abundance of *C. reniforme*, which dominates the assemblages only during this interval (Fig. 4). In Ecozone F-II, PC1 scores positive and PC2 scores negative values until 1790 ± 30 CE. Finally, in Ecozone F-I, PC1 values decrease to near zero values and then oscillate (Ecozone F-I.II) until a clear shift to negative values at ~1955 CE occurs (Ecozone F-I·I; Fig. 4).

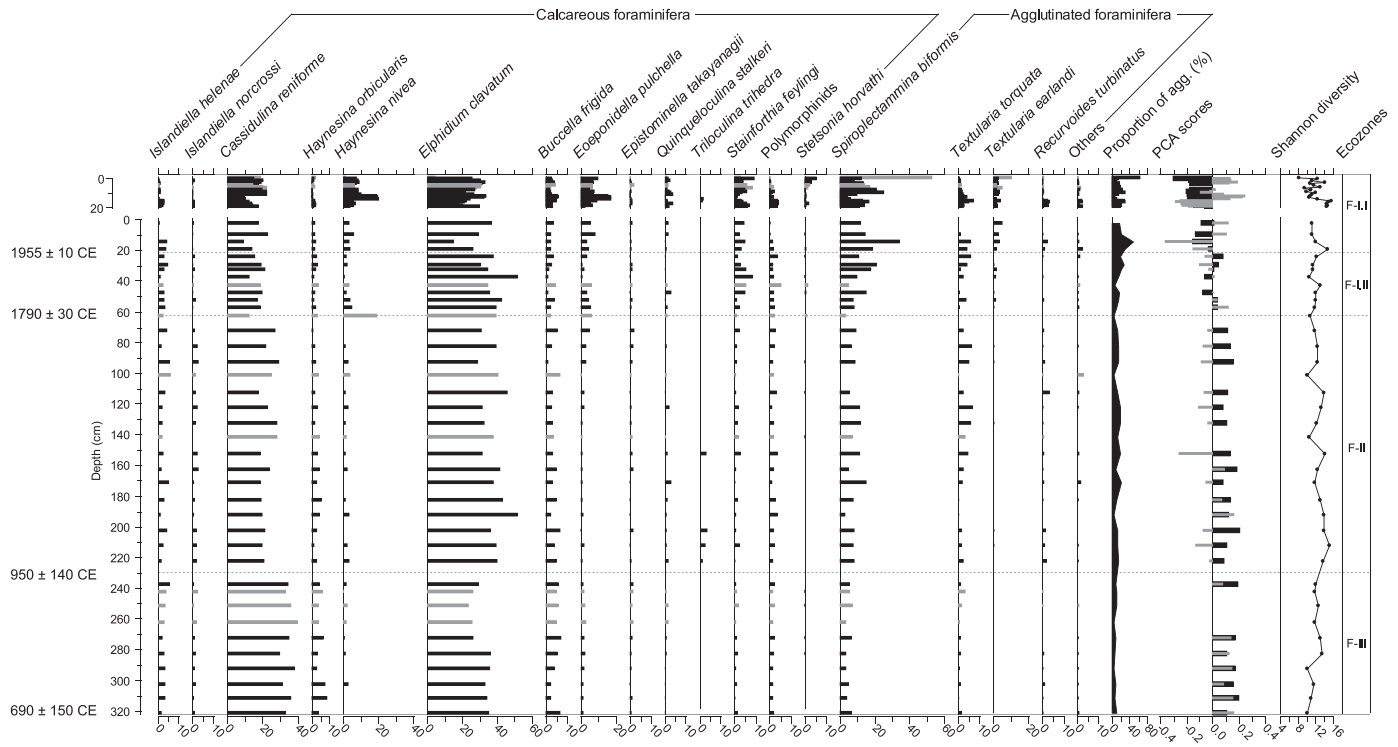

Fig. 4. Percentages of benthic foraminiferal taxa in the composite sediment sequence of cores PG2303–1/PG2303 as a function of depth (cm). The assemblages calculated with <300 foraminiferal tests are represented in gray. The principal component analysis (PCA) scores are represented by thick black bars (PC1) and thin gray bars (PC2). The ecozones were defined based on the PCA of the foraminiferal assemblages (see Fig. 5) and a shift in the dominant taxa.

4.4. Stable isotopes

The $\delta^{18}O$ of *Cassidulina reniforme* ($\delta^{18}O_{CR}$) mostly ranges from 1.5 to 2.5 ‰ (mean = 1.9 ± 0.3 ‰) throughout the composite sequence. It shows little variations nearly through ecozones F-III to F-II, after which large amplitude oscillations of ±1.0 ‰ occur (Fig. 6a). The stable carbon isotope of *C. reniforme* ($\delta^{13}C_{CR}$) records mean values of −1.6 ± 0.1 ‰.

The $\delta^{18}O$ of *Elphidium clavatum* ($\delta^{18}O_{EC}$) ranges between 0.2 and 1.6 ‰ before 1955 ± 10 CE (mean = 1.0 ± 0.2 ‰; Fig. 6a). Above, in Ecozone F-I.I, the $\delta^{18}O_{EC}$ shows a decrease accompanied by large amplitude oscillations of up to 4.0 ‰, with values ranging from −2.5 to 2.0 ‰. On the other hand, the $\delta^{13}C_{EC}$ is relatively uniform prior to 1790 ± 30 CE with a mean of −3.2 ± 0.1 ‰ and slowly decreases in the upper part of the sequence to reach values of −4.0 ± 0.1 ‰ at the core top (see raw data in Table S7).

4.5. Ostracod assemblages

In total, 19 ostracod taxa were identified. Among those, six are low salinity tolerant (LST) and 11 are euhaline (Table 2b; Fig. 7). The recurrent euhaline taxa are *Cytheropteron* spp., *Cytheropteron suzdalskyi*, and *Cytheropteron sulense* (cf. McDougall et al., 1986; Stepanova et al., 2019). *Paracyprideis pseudopunctillata* is the dominant LST taxa. The Shannon diversity index indicates that one to five ostracod genera compose the assemblages (Fig. 7). *Kotoracythere arctoborealis* occurs at three distinctive intervals, often accompanied by *Normanicythere leioderma*.

The PCA of the ostracod assemblages shows an opposite trend between two groups of species on the first axis, which explains 22% of the variance (PC1, Fig. 8; see Table 3 for the corresponding abbreviation names). The first group of PC1 includes *C. suzdalskyi*, *Cytheropteron brastadensis*, *Semicytherura complanata*, and *Cytheropteron* spp. scoring negatively, and the second group of PC1 is composed of *P. pseudopunctillata*, *K. arctoborealis*, *Cluthia cluthae*, *N. leioderma*, and *Rabilimis mirabilis* scoring positively. PC2, which explains 14% of the variance, is mainly characterized by *Heterocyprideis sorbyana* and *Loxoconcha venepidermoidea* scoring negative values in contrast to *S. complanata*, *C. cluthae* and *C. brastadensis* (Fig. 8). PC2 seems to discriminate ostracod taxa based on their salinity preference (Table 2b).

The Ecozones O-III, O-II, and O-I division is based on PC1. In Ecozone O-III, from 690 ± 150 to 1040 ± 135 CE, *Cytheropteron* spp. and *C. suzdalskyi* largely dominate the assemblages (57 ± 23%), which corresponds to negative PC1 scores and low species diversity (means of 2 ± 1; Figs. 7-8). In Ecozone O-II, PC1 values are positive with abundant *P. pseudopunctillata* (46 ± 20% of the assemblages). In Ecozone O-I, from 1920 ± 10 CE to the top of the record, PC1 values shift back to negative scores with the dominance of *Cytheropteron* spp. and *C. suzdalskyi* (65 ± 29%), and the species diversity drops (means of 2 ± 1). Ecozone O-I was subdivided into two subzones, based on marked negative PC2 scores after 1998 ± 8 CE associated with a notable increase of LST taxa occurrences (Fig. 7).

4.6. Ecozones and ecological shifts

The ostracod and foraminiferal ecozones are nearly similar in range, although the transitions from ecozones III to II, and from ecozones II to I, both occur later for ostracods than for the foraminifera (Figs. 4 and 7). The ecozones are compared in the summary Fig. 9, which is shown in function of depth due to the poorly constrained age model, especially prior to 1790 ± 30 CE (Fig. 2). Interpretations and comparisons with the literature are thus cautious for this interval. However, one important ecological shift at 1160 ± 130 CE was identified independently from the ecozones (see Section 5.2.2; Fig. 9). The two main ecological shifts identified are based on the more diverse and abundant foraminiferal assemblages, i.e. ecozones F-I.II and F-I.I, an interval where the age model is supported by additional radiogenic isotope data, and thus better constrained (i.e. after ~1800 CE; Figs. 2 and S2; Appendix A).

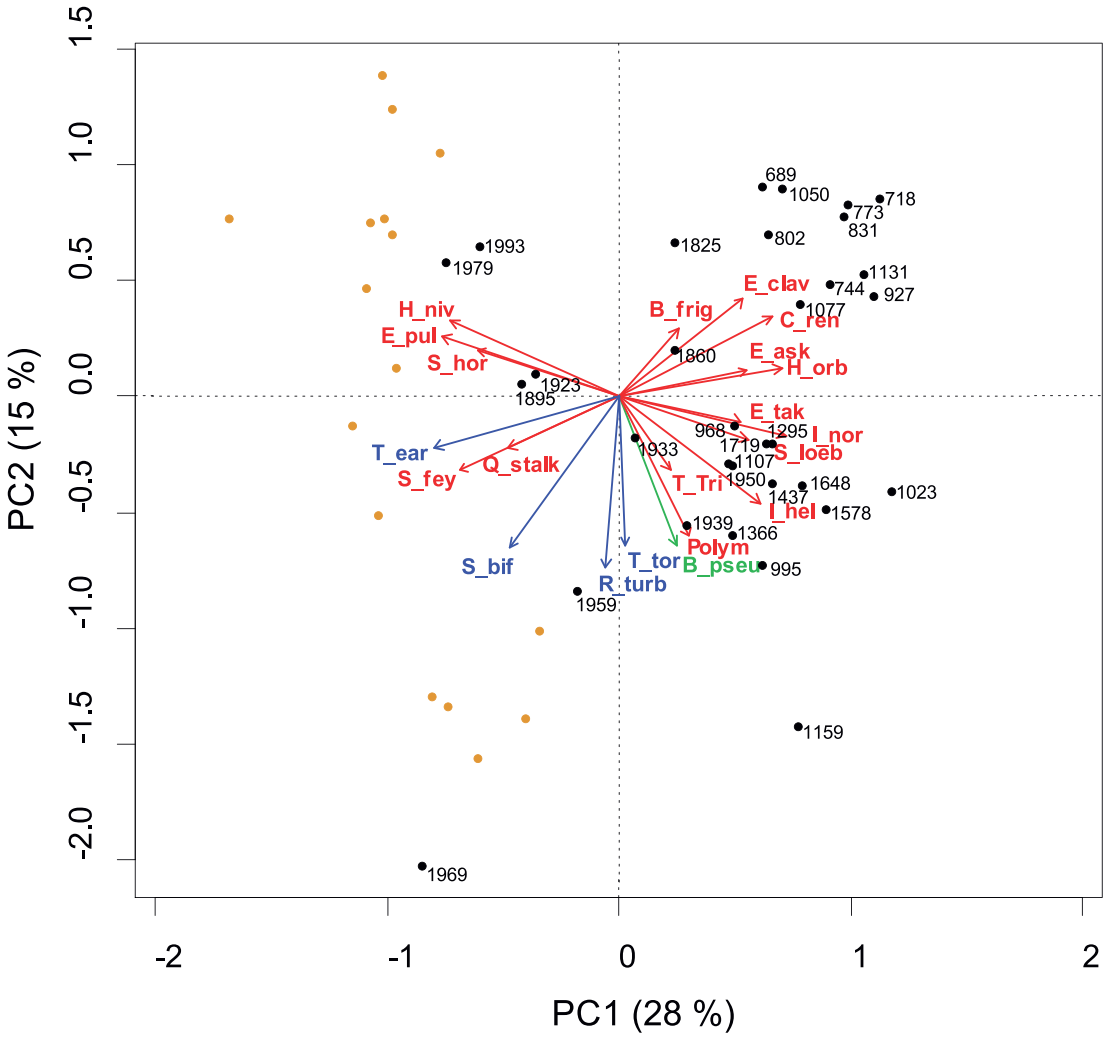

Fig. 5. PCA plot of foraminiferal assemblages in the composite sediment sequence of cores PG2303–1/PG2303 (black dots for piston core PG2303 samples and orange dots for the short gravity PG2303–1 core samples). Agglutinated foraminifera are shown in blue, the low-oxygen tolerant calcareous species *Bolivinellina pseudopunctata* (B_pseu) is in green, while the remaining calcareous species are shown in red. See Table 3 for the full names of the abbreviations used. (For interpretation of the references to colour in this figure legend, the reader is referred to the web version of this article.)

5. Discussion

5.1. Identification of environmental conditions from micropaleontological proxies

5.1.1. Variable salinities and turbidity on Arctic shelves

The nearshore PG2303–1/PG2303 cores were retrieved at a relatively shallow depth (32 m), around 20 m below the summer halocline (Mulligan et al., 2010; Fig. 1c), and within the propagation limit of the Mackenzie River plume (Wood et al., 2015). Our microfossil assemblages reflect the highly variable salinity, temperature, and sediment discharge typical of Arctic estuaries, with the occurrence of *Elphidium clavatum*, *Haynesina orbicularis,* and *Buccella frigida* (cf. Khusid and Korsum, 1996; Polyak et al., 2002). *Haynesina nivea*, which occurs throughout the sequence and records high percentages in the upper part of the core, is indicative of shallow environments with fluctuating low salinity (light blue in Fig. 9) and relatively warm waters (Madsen and Knudsen, 1994; Luoto et al., 2011; Voltski et al., 2015; Falardeau et al., 2023). The other common taxa include *Cassidulina reniforme*, *Islandiella helenae*, *Spiroplectammina biformis*, and *Textularia* spp. that are typical of Arctic Ocean shelves (Jennings and Helgadóttir, 1994; Scott et al., 2008a; Cage et al., 2021). They also include *Eoeponidella pulchella* that thrives in particularly nutrient-rich waters (Wollenburg and Kuhnt, 2000; Knudsen et al., 2008; Scott et al., 2008b; Falardeau et al., 2023), and together with *Epistominella takayanagii* (light green in Fig. 9), it may relate to enhanced productivity.

The presence of LST ostracods (light blue in Fig. 9; except *Paracyprideis pseudopunctillata*), notably *Heterocyprideis sorbyana* found in river-influenced shallow environments (Stepanova et al., 2007; Gemery et al., 2021), also suggests varying salinity.

Interestingly, the euhaline taxon *Cytheropteron sulense* reaches its highest abundance near the river mouths (Fig. S4b), similar to the tintinnid *Tintinnopsis fimbriata*, characteristic of sediment-loaded freshwaters (Echols and Fowler, 1973; Burkovsky, 1976; Rogers et al., 1981; Scott et al., 2008a; Falardeau et al., 2023). The relationship between *C. sulense* and estuaries is not clear yet, but this shallow-water taxon found at littoral depths may tolerate turbidity and feed on the seasonal supply of food from river discharges.

5.1.2. Relationships to sea ice and food requirements

The nearshore study site is influenced by sea ice with land-fast ice that persists for nearly 9 months per year, from October to June (Carmack and Macdonald, 2002). The dominance of *Cassidulina reniforme* and *Elphidium clavatum* is compatible with such an environment and often constitute sea-ice proximal assemblages in fjords and glacial tongues (Hald and Korsun, 1997; Korsun and Hald, 2000; Jennings et al.,

Table 3
List of abbreviations used for foraminiferal and ostracod taxa in the Figs. 5 and 8.

Benthic foraminifera:	
B_frig	*Buccella frigida*
B_pseu	*Bolivinellina pseudopunctata*
C_ren	*Cassidulina reniforme*
E_ask	*Elphidium asklundi*
E_clav	*Elphidium clavatum*
E_pul	*Eoeponidella pulchella*
E_tak	*Epistominella takayanagii*
H_niv	*Haynesina nivea*
H_orb	*Haynesina orbicularis*
I_hel	*Islandiella helenae*
I_nor	*Islandiella norcossi*
Polym	Polymorphinids
Q_stalk	*Quinqueloculina stalkeri*
R_turb	*Recurvoides turbinatus*
S_bif	*Spiroplectammina biformis*
S_fey	*Stainforthia feylingi*
S_hor	*Stetsonia horvathi*
S_loeb	*Stainforthia loeblichi*
T_ear	*Textularia earlandi*
T_tor	*Textularia torquata*
T_Tri	*Triloculina trihedra*
Ostracods:	
C_bic	*Cytheropteron biconvexa*
C_bras	*Cytheropteron brastadensis*
C_clut	*Cluthia cluthae*
C_ela	*Cytheropteron elaeni*
C_spp	*Cytheropteron* spp.
C_sul	*Cytheropteron sulense*
C_suz	*Cytheropteron suzdalskyi*
E_del	*Eucytherura delineata*
H_sorb	*Heterocyprideis sorbyana*
K_arcto	*Kotoracythere arctoborealis*
L_ven	*Loxoconcha venepidermoidea*
N_lei	*Normanicythere leioderma*
P_pseu	*Paracyprideis pseudopunctillata*
R_glob	*Roundstonia globulifera*
R_mir	*Rabilimis mirabilis*
S_comp	*Semicytherura complanata*

2020). The ostracod *Semicytherura complanata,* which records maximum abundance in polynyas of the Bering and Siberian shelves (Barber and Massom, 2007; Fig. S4f), may indicate enhanced sea-ice formation and brine rejections (Stepanova et al., 2003). The ostracod *Paracyprideis pseudopunctillata*, although also tolerant to low salinity (light blue in Fig. 8), may relate to an environment characterized by brine rejections (Gemery et al., 2021). Hence, *P. pseudopunctillata* is widely distributed along the Arctic nearshore areas, particularly where new sea ice is formed year-round on the East Siberian shelf (Fig. S4e). *P. pseudopunctillata* accompanied by *S. complanata* and *Cluthia cluthae* forms an assemblage similar to those of Hanna Shoal, NW Alaska (Fig. 1a), where frigid winter waters (dark blue in Fig. 9; Gemery et al., 2021) are accompanied with brine rejections. Furthermore, *Stainforthia feylingi* has a connection with sea ice as it typically thrives in the high-productivity areas near sea-ice margins (dark green in Fig. 9; Seidenkrantz, 2013).

Textularia earlandi and *Stetsonia horvathi* usually dominate oligotrophic waters under permanent sea-ice cover (Wollenburg and Mackensen, 1998; Wollenburg and Kuhnt, 2000; Jennings et al., 2020). However, in this study, we propose that the presence of *T. earlandi* and *S. horvathi* may be controlled by their feeding strategy. Both taxa can feed on complex organic carbon or bacterial degradation products that constitute food of poor quality (Alve, 2010; Jennings et al., 2020). *Quinqueloculina stalkeri* is a more bacterial feeder than a fresh algal feeder and can tolerate high turbidity (Guilbault et al., 2003). Hence, the three taxa, *T. earlandi*, *S. horvathi,* and *Q. stalkeri*, are here grouped as bacterial/complex carbon feeders (brown in Fig. 9). The bacterial/complex carbon feeders may represent opportunistic behavior taking advantage of increased food supply regardless of the food type (cf. also Mäkelä et al., 2018). Intervals of more depleted $\delta^{13}C$ in the tests of benthic foraminifera may point to enhanced organic carbon fluxes and remineralization (Mackensen, 2008).

5.1.3. The shelf-break waters

The shelf-break waters, which are mainly derived from Pacific waters and the slightly saltier and warmer Atlantic waters (Lin et al., 2020), are important components of the Herschel Basin hydrography. They upwell along the margin and fill the bottom of the basin (Williams and Carmack, 2012). These water masses have a more oceanic signatures and may be associated with species that prefer cool stable saline bottom waters such as *Islandiella norcrossi* (cf. Polyak et al., 2002), a species which has been found associated with chilled Atlantic Water (Rytter et al., 2002; Cage et al., 2021; Seidenkrantz et al., 2021), and *Cassidulina reniforme* (cf. Polyak et al., 2002; Scott et al., 2008a). The occurrence of *Triloculina trihedra*, even in relatively low numbers, also suggests inflow of stable and saline bottom waters as miliolids thrive in such conditions (Murray, 1991; Polyak et al., 2002). Moreover, *T. trihedra* was previously found in assemblages dominated by the Atlantic-water indicator *Cassidulina neoteretis cf.* (Seidenkrantz et al., 2021) in the Kara Sea (Husum et al., 2015) and the Eurasian Basin (Wollenburg and Mackensen, 1998). However, although these taxa suggest stable and saline bottom waters, they do not necessarily provide evidence of Atlantic waters in the Herschel Basin.

Kotoracythere arctoborealis today reaches its maximum abundance in the Bering and Chukchi Seas (Fig. S4c; Gemery et al., 2021; orange in Fig. 9), while *Normanicythere leioderma* is found in relation to productive bottom waters in the Bering-Chukchi-Beaufort Seas (Fig. S4d; Gemery et al., 2021), and often co-occurs with *K. arctoborealis* (Fig. 7). Together, the intermittent occurrence of these species in our record may indicate variable presence of nutrient-rich Pacific waters (green and orange in Fig. 9) and thus, that influx of Pacific-sourced waters has occurred in pulses in the Herschel Basin during the last millennium (orange in Fig. 9); this may be partly due to its bathymetric features. Hence, intensified penetration of shelf-break water masses into the basin may occur during events of particularly favorable climatic conditions for upwelling on the Beaufort Sea shelf and/or for the eastward flow of Pacific waters.

5.2. History of environmental conditions prior to ~1800 CE

5.2.1. Influence of oceanic waters in the Herschel Basin from ~700 to 1150 CE

In Ecozone F-III, the dominance of *Cassidulina reniforme* and the occurrence of *Islandiella norcrossi* (Fig. 4) suggest influx of relatively saline bottom waters from the open shelf (see discussion in Section 5.1.3). The enhanced inflow of oceanic waters persisted slightly into Ecozone F-II as *Triloculina trihedra* relative abundance increases from 950 ± 140 to 1040 ± 135 CE (Fig. 9). Yet, the frequent occurrence of *Cytheropteron sulense* through Ecozone O-III (~690–1040 CE; Figs. 7, S4b) rather suggests estuarine-like conditions (Section 5.1.1) with episodes of freshwater discharge consistent with the abundance of *Haynesina orbicularis* and *Buccella frigida* (Fig. 4; Polyak et al., 2002). Altogether, the foraminiferal and ostracod assemblages thus suggest a combination between relatively high inflow of oceanic waters as well as relatively strong outflow of lower-salinity waters presumably derived from river runoff and/or snow and sea-ice melt. Similarly, oscillations in the oxygen stable isotope signals of ostracod valves and in the agglutinated foraminiferal abundances in the more offshore core HLY1302 (Fig. 1b) suggest fluctuating salinity and temperature in bottom waters between 800 and 1200 CE (Gemery et al., 2023).

In contrast, the $\delta^{18}O_{EC}$ and $\delta^{18}O_{CR}$ are relatively stable and oscillate close to 1.0 ‰ and 1.8 ‰, respectively, through Ecozone F-III (Fig. 6a). Based on the strong linear relationship between $\delta^{18}O$ of seawater and salinity in the Herschel Basin, these values would correspond to a

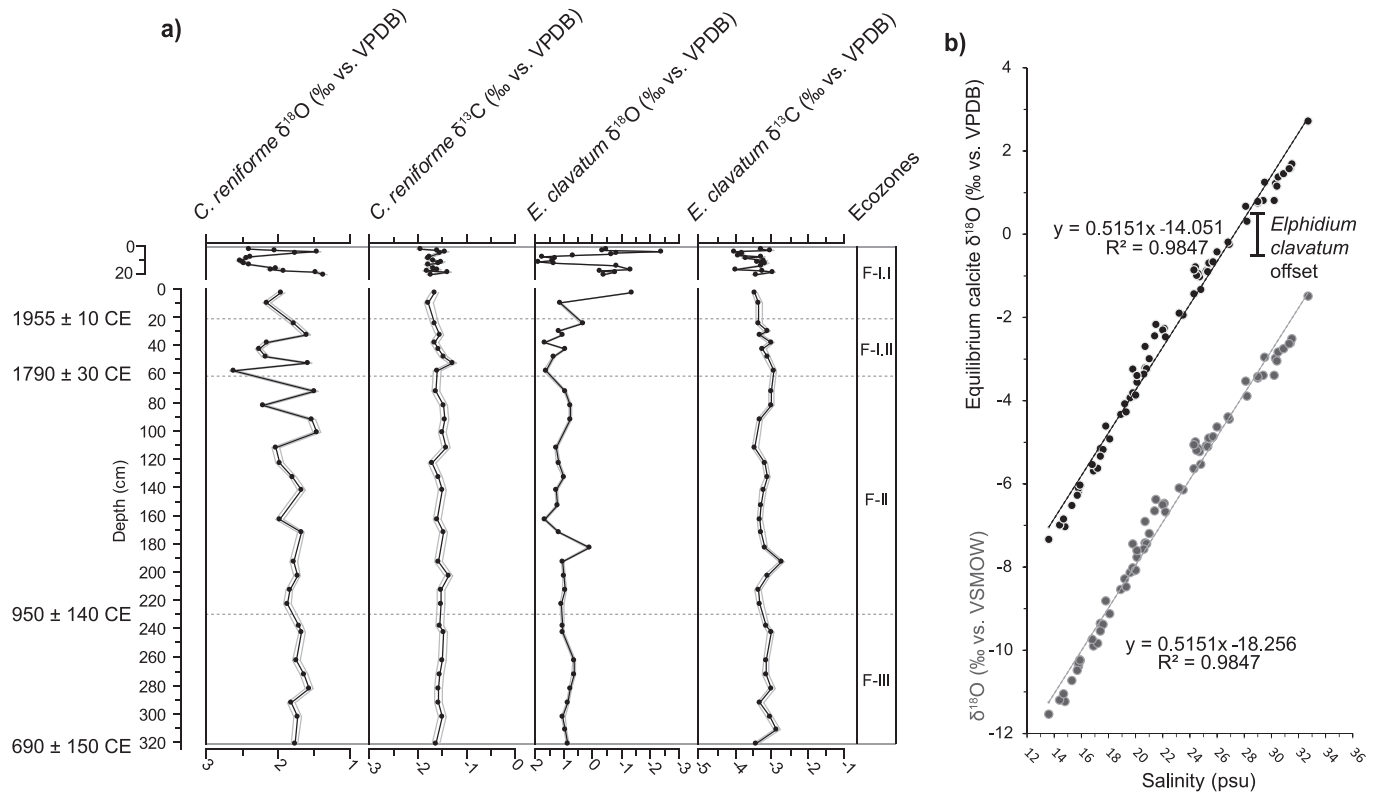

Fig. 6. a) Stable isotope ratios ($\delta^{18}O$ and $\delta^{13}C$) of *Elphidium clavatum* and *Cassidulina reniforme* in the composite sediment sequence of cores PG2303–1/PG2303 as a function of depth (cm). The thin lines surrounding the main curves illustrate the analytical uncertainty. b) The equilibrium calcite $\delta^{18}O$ as a function of salinity (black dots; Table S7) calculated from $\delta^{18}O$ in the water column measured in the Herschel Basin at different depths in summer 2015 (gray dots; Table S8). A negative offset of 1.0 ‰ for *Elphidium clavatum* is depicted.

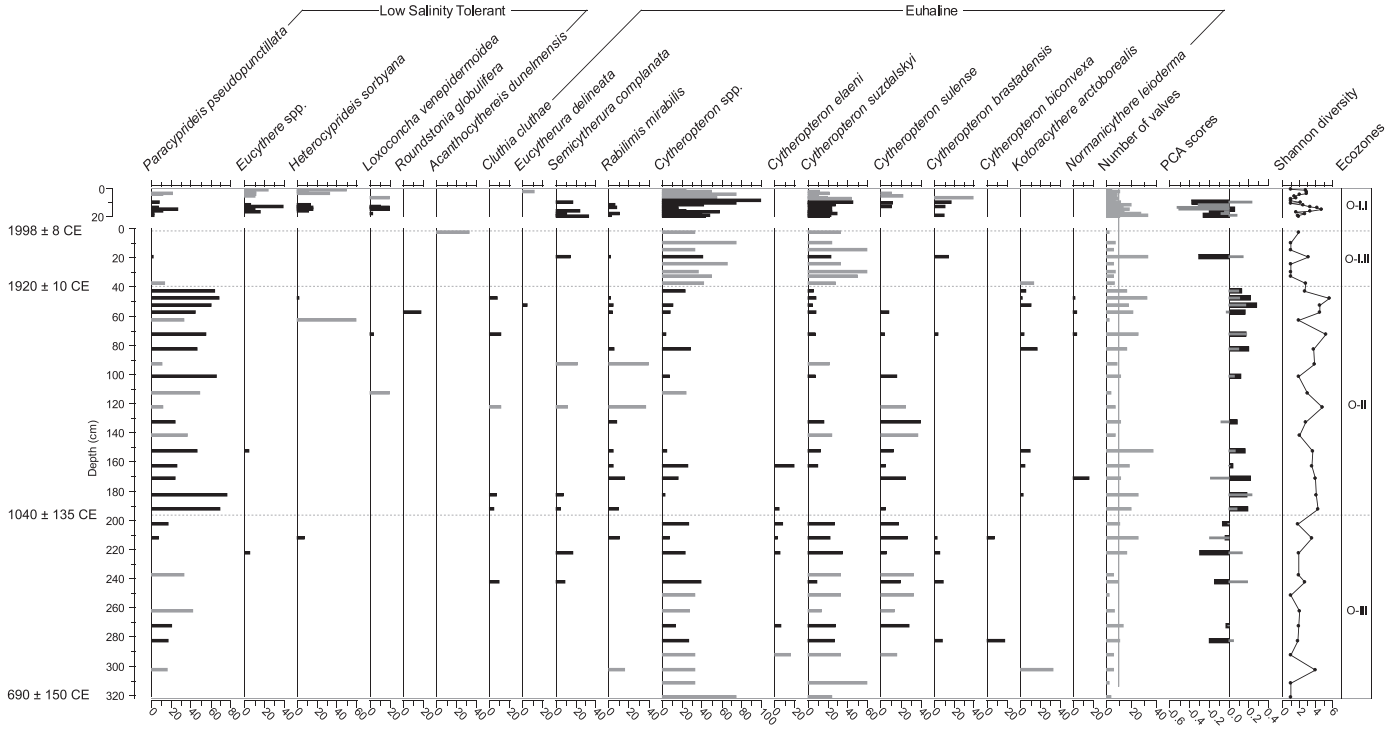

Fig. 7. Relative abundances of ostracod taxa in the composite sediment sequence of cores PG2303–1/PG2303 as a function of depth (cm). The assemblages calculated with <10 ostracod valves are represented in gray. The principal component analysis scores are represented by thick black bars (PC1) and thin gray bars (PC2). The ecozones were defined based on the PCA of the ostracod assemblages (see Fig. 8).

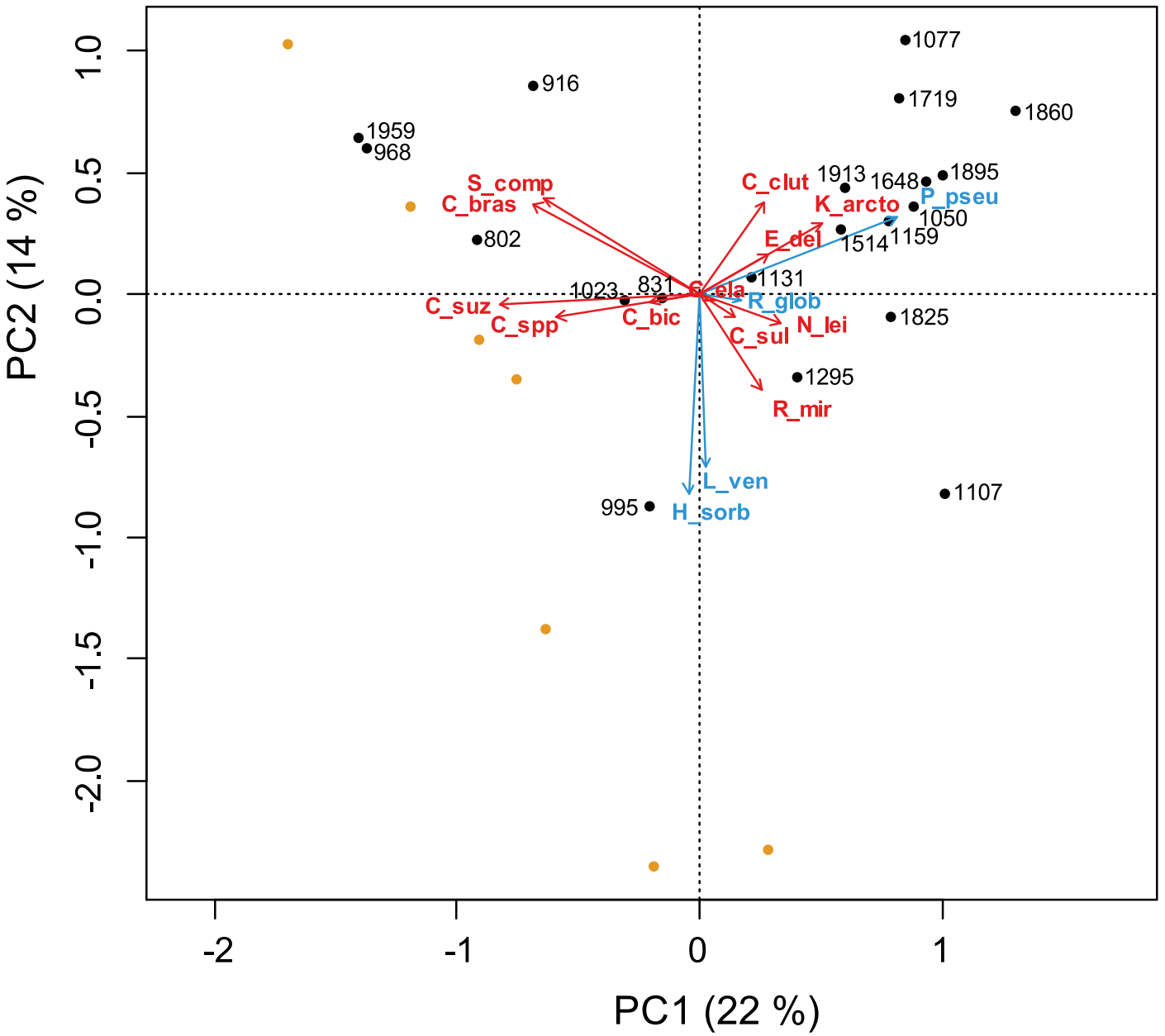

Fig. 8. PCA plot of the ostracod assemblages in the composite sediment sequence of cores PG2303–1/PG2303 (black dots for piston core PG2303 samples and orange dots for the short gravity PG2303–1 core samples). The LST taxa are in blue and the euhaline taxa are in red. See Table 3 for the full names of the abbreviations used. (For interpretation of the references to colour in this figure legend, the reader is referred to the web version of this article.)

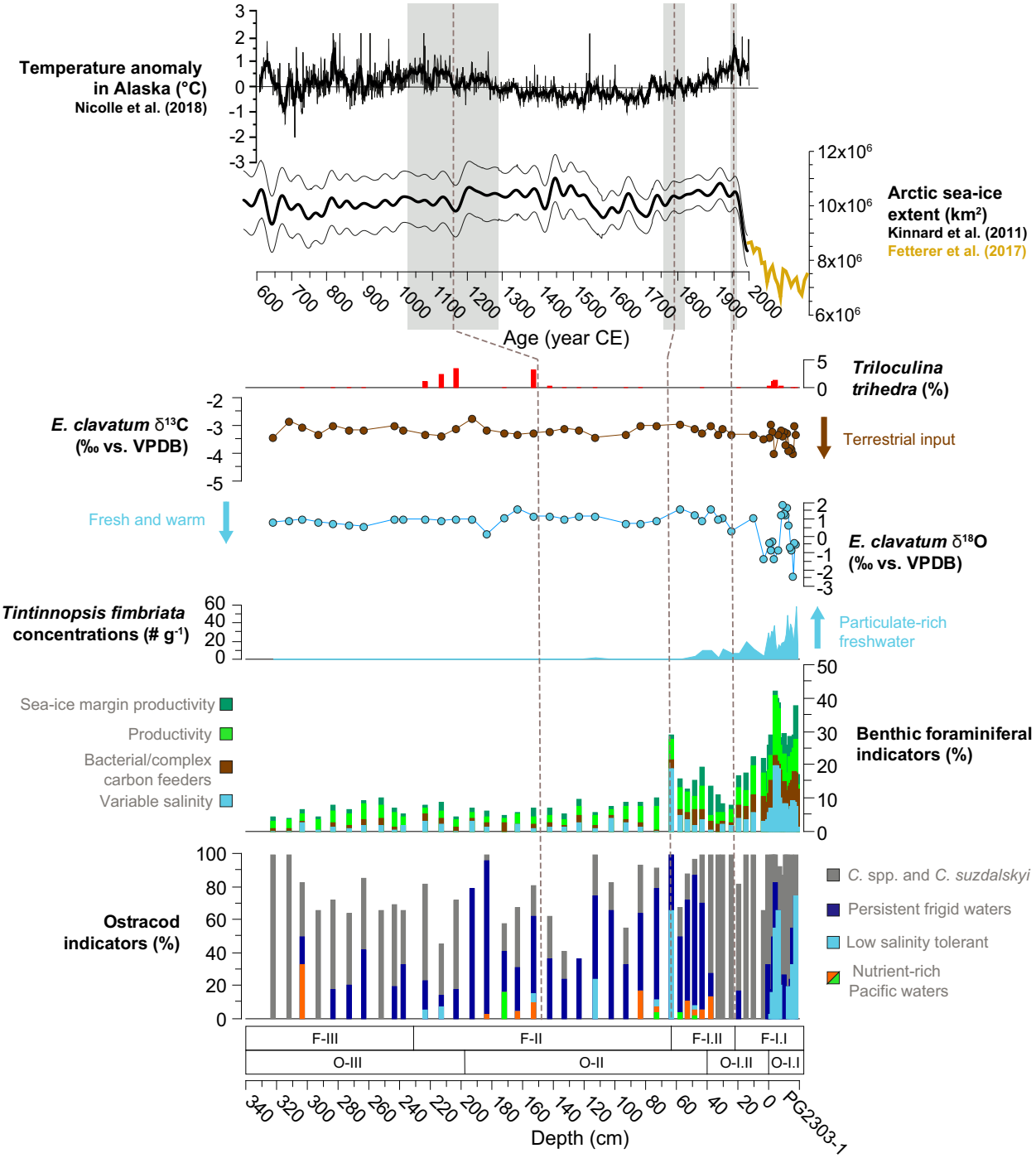

Fig. 9. Summary figure of paleoecological data from the Herschel Basin site PG2303 in function of depth (cm) compared with existing data of temperature anomalies in Alaska (Nicolle et al., 2018) and summer sea-ice extent in the Arctic Ocean from 600 to 2000 CE (Kinnard et al., 2011; black line) with a close-up from 2000 to 2022 CE (Fetterer et al., 2017; yellow line) in function of age (year CE). Three important shifts are identified: at 1160 ± 130 CE, a transition to particularly cold conditions, and at 1790 ± 30 CE and at 1955 ± 10 CE to mark the early onset and the acceleration of the modern warming, respectively. For the ostracod indicators (cumulative percentages): Pacific waters (orange) = *Kotoracythere arctoborealis*; Productivity (light green) = *Normanicythere leioderma*; Low salinity tolerant (light blue) = *Heterocyprideis sorbyana*, *Loxoconcha venepidermoidea* and *Eucythere* spp.; Persistent frigid waters (dark blue) = *Paracyprideis pseudopunctillata*, *Cluthia cluthae* and *Semicytherura complanata*. For the benthic foraminiferal indicators (cumulative percentages): Variable salinity (light blue) = *Haynesina nivea*; Bacterial/complex organic carbon feeders (brown) = *Textularia earlandi*, *Stetsonia horvathi* and *Quinqueloculina stalkeri*; Productivity (light green) = *Eoeponidella pulchella* and *Epistominella takayanagii*; Sea-ice margin productivity (dark green) = *Stainforthia feylingi*. *Triloculina trihedra* refers to cool and stable saline waters (red). (For interpretation of the references to colour in this figure legend, the reader is referred to the web version of this article.)

salinity of ~31 psu if assuming a negative offset of 1.0 ‰ for *Elphidium clavatum* (Fig. 6b; Erlenkeuser and von Grafenstein, 1999; Polyak et al., 2003). This is within the current mean annual (summer to winter) range for the bottom water salinity (ranging 28–32 psu; Mulligan et al., 2010; referred to as Polar Mixed Layer). Thus, the temporal resolution captured by the $\delta^{18}O_{EC}$ and $\delta^{18}O_{CR}$ is likely not sufficient to be used as indicators of summer bottom water salinity variations in this interval (cf. Gemery et al., 2023).

At 1040 ± 135 CE, the presence of *Paracyprideis pseudopunctillata* accompanied by *Cluthia cluthae* and *Semicytherura complanata* supports persistent frigid and saline bottom waters through Ecozone O-II (Section 5.1.2). Concurrently, the presence of *Rabilimis mirabilis* (Fig. 7) may indicate the development of stable cold and saline bottom waters as this species thrives in the upper limit of the Arctic Ocean halocline (Cronin et al., 2022). Such conditions may suggest enhanced sea-ice formation and brine rejections leading to poorly mixed bottom waters and strong stratification. The increased occurrence of the calcareous low-oxygen tolerant species *Bolivinellina pseudopunctata* (Alve and Bernhard, 1995; Patterson et al., 2000) combined with the relatively high frequencies of agglutinated foraminifera in Ecozone F-II (Figs. 4-5; Table S6), suggests episodes of reduced bottom-water ventilation and increased rejection of corrosive brines (Nardelli et al., 2023), respectively. However, conditions on the continental shelf were likely still favorable for biological productivity with continuous influence of shelf-break waters until 1160 ± 130 CE as suggested from the occurrence of Pacific water indicators (orange and green, Fig. 9).

5.2.2. The culmination of a regional cooling between ~1150 and 1650 CE

Afterwards, for a few hundred years, from 1160 ± 130 CE to 1650 ± 50 CE, there is no indication of strong oceanic inflow (Section 5.1.3). We associate this interval with the coldest phase of our record. It was likely marked by dense sea-ice cover, limited upwelling to the shelf (Schulze and Pickart, 2012), and low productivity as illustrated by low microfossil abundances and fluxes (Fig. 3). This interval was characterized by low sediment accumulation rates (Fig. 3), which concurs with a pervasive sea-ice cover limiting sediment supply from coastal erosion, floating ice, or the spreading of the Mackenzie River plume. The transition towards these cold conditions at 1160 ± 130 CE is probably synchronous with a decrease in air temperatures over Alaska (~1150 CE; cf. Nicolle et al., 2018; Fig. 9) and with an increase of Arctic sea-ice extent (Kinnard et al., 2011; Fig. 9). This time period also approximately corresponds to the period of the Little Ice Age (Mann et al., 2009).

5.2.3. The early decline of harsh climate conditions near the coast, ~1650–1800 CE

Towards the end of Ecozone F-II, at 1650 ± 50 CE, bio-productivity increased slightly (light green, Fig. 9) while Pacific waters were reintroduced (orange, Fig. 9). The combination of productivity and influx of Pacific waters suggests longer sea-ice-free seasons and recurrence of milder conditions on the Beaufort Sea shelf. This agrees with the conclusions of Richerol et al. (2008), who documented high cyst concentrations of phototrophic dinoflagellate taxa as early as ~1624 CE in a site close to the coast in the Mackenzie Trough (core 912A, Fig. 1b), and about 300 years earlier than what was recorded at more offshore study sites (cores 906B, 803BC and HLY1302; Fig. 1b; Richerol et al., 2008; Bringué and Rochon, 2012; Gemery et al., 2023). Notably, the $\delta^{18}O_{CR}$ signal starts to oscillate of about 1.0 ‰ at approximately the same time (~1580 CE) in our record (end of Ecozone F-II; Fig. 6a). These oscillations may suggest larger amplitude salinity variations of ±2 psu (Fig. 6), albeit still within the present seasonal salinity variations (Mulligan et al., 2010).

5.3. The modern warming after ~1800 CE

5.3.1. The environmental impact of the gradual warming from ca 1800 to 2000 CE

At 1790 ± 30 CE, both benthic foraminiferal and ostracod records suggest a short but strong freshwater pulse (light blue; Fig. 9). Bringué and Rochon (2012) also reported a low salinity event at 1790 CE (core 803BC; Fig. 1b), which they linked to a release of freshwater accumulated by the Beaufort Gyre, due to a shift from anticyclonic to cyclonic regime. Shortly after this freshwater pulse, the concentrations of *Tintinnopsis fimbriata*, which lives at depths of 0–40 m in the water column (Paranjape, 1987), increased significantly at our study site, which suggests enhanced inflow of fresh and sediment-loaded waters (Echols and Fowler, 1973; Scott et al., 2008a; Falardeau et al., 2023; light blue, Fig. 9). The high accumulation rates (Fig. 3) also point to high sediment supply, which is in agreement with increased abundance of *Spiroplectammina biformis* (Fig. 4), a taxon tolerant to rapid sedimentation and turbid meltwater (Jennings and Helgadóttir, 1994). Concurrently, enhanced input of terrestrial organic carbon is illustrated by the increase in bacterial/complex feeders (brown, Fig. 9; Section 5.1.2).

The input of terrestrial particles may be linked to a westward spread of the Mackenzie River plume (Ehn et al., 2019; Juhls, 2021) or could alternatively originate from coastal erosion (Grotheer et al., 2020; Jong et al., 2020). Fluvial inputs and coastal erosion can both be linked to a more extended open-water season with a more rapid response of the river plume to wind stress (Mulligan and Perrie, 2019). Increased permafrost degradation in response to an enhanced wave impact under ice-free conditions may also be a cause (Overeem et al., 2011; Günther et al., 2015; Mioduszewski et al., 2018). Moreover, longer ice-free seasons would facilitate the recorded increase in biological productivity (light and dark green, Fig. 9). Altogether, the low and variable salinity in surface/subsurface waters (light blue, Fig. 9) and the increased terrestrial organic input and productivity (brown and green, Fig. 9) illustrate the beginning of the modern warming at the onset of foraminiferal Ecozone F-I (Fig. 9).

A break-up of the cold and saline bottom winter waters at around 1920 ± 10 CE is inferred from the ostracod assemblages mainly as *Paracyprideis pseudopunctillata* decreases drastically (Figs. 7 and 9). This coincides with the reduced abundances of *Islandiella norcrossi*, which prefers stable saline waters (after sample 43–42 cm; Fig. 4; Cage et al., 2021; Falardeau et al., 2023). Thus, this transition may relate to enhanced seasonal mixing/renewal of the bottom waters, causing increased variability of the bottom-water salinity, which is often characterized by open waters in nearshore settings. A sea-ice break-up earlier in the summer season, and thus a more extended open-water season, would coincide with enhanced sea-ice margin productivity, as it is also suggested by increased abundance of the foraminifera *Stainforthia feylingi* (Figs. 4 and 9; Section 5.1.2). Reduced summer sea-ice cover may have favored offshore inputs of terrestrial matter as reworked palynomorphs peaked on the slope of the Mackenzie shelf around 1920 CE (core 803BC; Fig. 1b; Bringué and Rochon, 2012). The microfaunal transition around 1920 ± 10 CE coincides with the regional warming inferred from other records on land using varves (Bird et al., 2009), pollen (Wolter et al., 2017), and tree-ring series (Porter et al., 2013).

All the above listed indicators of warming reach maximum values after 1955 ± 10 CE (Ecozone F-I·I; Fig. 9), which could be the regional signature of the main onset of anthropogenic warming. The 1955 CE shift corresponds to a significant decrease in Arctic sea-ice extent (Kinnard et al., 2011; Fetterer et al., 2017; Fig. 9) and accelerated atmospheric warming (Anchukaitis et al., 2013; Porter et al., 2013; Nicolle et al., 2018; Fig. 9). The timing of the onset and the acceleration of the modern warming are consistent with those in the synthesis of Abram et al. (2016) at 1830 CE and 1930 CE, respectively, for the Arctic region.

5.3.2. The post-2000 CE environmental conditions

After ~2000 CE, the Herschel Basin bottom waters are characterized by low salinity excursions, expressed by large $\delta^{18}O_{EC}$ oscillations, abundant *Haynesina nivea* and LST ostracods (light blue, Fig. 9). The $\delta^{18}O_{EC}$ signal would correspond to high salinity variations ranging from 24.5 to 33 psu (Fig. 6a, b). Although, the large amplitudes might to some extent be an artifact of changing internal offsets of *Elphidium clavatum* in low salinities (Polyak et al., 2003; Bauch et al., 2004), the peaks of depleted $\delta^{18}O_{EC}$ still strongly suggest episodes of low salinity. The low salinity fluctuations observed at depth in the basin may be explained by enhanced vertical mixing under seasonal sea-ice-free conditions (Rainville and Woodgate, 2009), in agreement with the low summer sea-ice concentrations recorded after ~2000 CE (Fetterer et al., 2017; Falardeau et al., 2023). Hence, low sea-ice leading to the increased impact of

storms (Mioduszewski et al., 2018) probably have fostered mixing and turbulence in the water column.

Stronger easterly winds have been recorded at the Komakuk Beach weather station after 1996 CE (Fig. 1b; Environment Canada, 2020). Such winds foster the spreading of the Mackenzie River plume, particularly during ice-free conditions (Wood et al., 2015; Mulligan and Perrie, 2019). This could explain the high *Tintinnopsis fimbriata* concentrations (Figs. 3 and 9). Concomitantly, easterly winds favoring upwelling of cold and saline subsurface waters (Carmack and Macdonald, 2002; Pickart et al., 2011) may have resulted in salinity variations (light blue, Fig. 9) and enhanced productivity (light green, Fig. 9; Tremblay et al., 2011, 2012; Pickart et al., 2013). Easterly winds are also associated with sediment resuspension and turbidity around Herschel Island-Qikiqtaruk (Klein et al., 2019), in agreement with increased erosion rates recorded since 2000 CE (Jones et al., 2009; Obu et al., 2016; Radosavljevic et al., 2016), which may have contributed to maximum terrestrial inputs in accord with the depleted $\delta^{13}C_{EC}$ signal (Figs. 6a and 9; Polyak et al., 2003; Mackensen, 2008; Grotheer et al., 2020).

6. Conclusions

The unique setting of the Herschel Basin as a sedimentary depocenter with high accumulation rates in the nearshore zone of the western Canadian Arctic yields microfossil records that allow us to reconstruct changes in the nearshore environments of the Canadian Beaufort Sea at high temporal resolution over the last 1300 years. The foraminiferal, ostracod, and tintinnid data, together with the isotopic composition of foraminiferal tests, provide complementary information about bottom (benthic foraminifera and ostracods) and surface (tintinnids) water conditions (temperature, salinity), sea-ice coverage, and organic matter fluxes through productivity and terrestrial input.

The records also enable inferences about regional climate changes, which appear related to terrestrial temperature anomalies in Alaska and sea-ice cover extent in the Arctic Ocean. A particularly cold interval was recorded between 1150 CE and 1650 CE as marked by persistent frigid winter waters, together with hampered upwelling of shelf-break waters, low productivity, and limited sediment supply to the basin, most probably in response to heavy annual sea-ice cover.

The most salient feature of this study is the regional signature of the ongoing global climate warming that was recorded as early as 1790 ± 30 CE, but increased sharply after 1955 ± 10 CE, likely in response to the ongoing anthropogenic forcing. It seems to coincide with the onset and emergence of the industrial-age warming, as evidenced by Abram et al. (2016) on an hemispheric scale and more regionally, in Alaska, as shown by Nicolle et al. (2018).

The impacts of climate changes include salinity variations in surface water that may be caused by the Mackenzie River plume extent and sea-ice melt. They also include higher terrestrial input with regards to the Mackenzie River plume and coastal erosion. These impacts reach maxima after 2000 CE and are marked by particularly high fluctuations of bottom water conditions because of intensified vertical mixing. All the above-listed impacts of climate change are probably directly or indirectly related to reduced summer sea-ice cover. Finally, we can conclude that the magnitude of these impacts in the post 2000 CE interval is unprecedented over the last 1300 years and thus over the history of traditional harvesting in the nearshore waters of the Canadian Beaufort Sea by the Inuvialuit and their ancestors.

CRediT authorship contribution statement

Jade Falardeau: Conceptualization, Formal analysis, Investigation, Writing – original draft, Visualization, Project administration, Funding acquisition. **Anne de Vernal:** Conceptualization, Writing – review & editing, Supervision, Funding acquisition. **Marit-Solveig Seidenkrantz:** Writing – review & editing, Supervision. **Michael Fritz:** Conceptualization, Resources, Writing – review & editing, Supervision, Funding acquisition. **Thomas M. Cronin:** Writing – review & editing. **Laura Gemery:** Writing – review & editing. **André Rochon:** Writing – review & editing. **Vladislav Carnero-Bravo:** Investigation, Writing – review & editing. **Claude Hillaire-Marcel:** Writing – review & editing. **Christof Pearce:** Methodology, Software, Writing – review & editing. **Philippe Archambault:** Conceptualization, Writing – review & editing, Supervision.

Declaration of Competing Interest

The authors declare that they have no known competing financial interests or personal relationships that could have appeared to influence the work reported in this paper.

Data availability

The data used in this study can be found in the supplementary material except for the raw counts of microfossils and the chronology of core PG2303–1, which are published in Falardeau et al. (2023). We are also in the process of publishing the raw counts of microfossils and the stable isotope data from cores PG2303–1 and PG2303 in PANGAEA.

Acknowledgements

We acknowledge the Fonds de Recherche du Quebec Nature et Technologies (FRQNT) that funded JF through scholarships. This study was also possible thanks to Natural Sciences and Engineering Research Council (NSERC) of Canada funds through a Discovery grant to AdV and a CREATE grant to ArcTrain [grant no. 432295]. We wish to thank the Geotop Research Center for equipment and laboratory access and more personally, to Jean-François Hélie and Agniezska Adamowicz-Walczak for their help and support in the preparation of the stable isotope analyses. TC and LG are funded by the U.S. Geological Survey, Climate Research and Development Program. Any use of trade, firm, or product names is for descriptive purposes only and does not imply endorsement by the U.S. Government. MSS is funded by the Independent Research Fund Denmark [grant no. 0135-00165B; GreenShelf] and the European Union's Horizon 2020 research and innovation program [grant agreement no. 869383; ECOTIP]. MF and JF have received financial support by the Nunataryuk project, which is funded by the European Union's Horizon 2020 research and innovation program [grant no. 773421]. VCB received a National Council of Science and Technology (CONACYT) postdoc grant from Mexico [CVU no. 174856]. We express our thanks to the Yukon Territorial Government and the Yukon Parks (Herschel Island – Qiqiktaruk Territorial Park). The authors acknowledge the support of the Aurora Research Institute (ARI, Inuvik) for the field component. We finally wish to thank all the people that contributed to the realization of this study: George Tanski, Jan Kahl and Boris Biskaborn who supported sediment coring; Margaux Rougier and Estelle Allan for the ostracod distribution maps and support with Ocean Data View, respectively; Bianca Fréchette for her advice in statistical analyses; Diogo Barnetche for the location of equipment at the Département des Sciences de la Terre; Tiffany Audet and Anna To for micropaleontological sample preparations; and Philippe Roberge for the grain size analyses.

Appendix A. Supplementary data

Supplementary data to this article can be found online at https://doi.org/10.1016/j.palaeo.2023.111670.

References

Abram, N.J., McGregor, H.V., Tierney, J.E., Evans, M.N., McKay, N.P., Kaufman, D.S., the PAGES 2k Consortium (Thirumalai K., Martrat B., Goosse H., Phipps S.J., Steig E.J., Kilbourne, K.H., Saenger, C.P., Zinke J., Leduc G., Addison J.A., Mortyn P.G., Seidenkrantz M.-S., Sicre M.A., Selvaraj K., Filipsson, H.L., Neukom, R., Gergis, J.,

Mark A.J., Curran M.A.J., Gunten L.), 2016. Early and asynchronous onset of industrial-era warming. Nature 536, 411–415. https://doi.org/10.1038/nature19082.
Agatha, S., 2008. Redescription of the tintinnid ciliate Tintinnopsis fimbriata Meunier, 1919 (Spirotricha, Choreotrichida) from coastal waters of Northern Germany. Denisia 23, 261–272.
Alve, E., 2010. Benthic foraminiferal responses to absence of fresh phytodetritus: a two-year experiment. Mar. Micropaleontol. 76, 67–75.
Alve, E., Bernhard, J.M., 1995. Vertical migratory response of benthic foraminifera to controlled oxygen concentrations in an experimental mesocosm. Mar. Ecol. Prog. Ser. 116, 137–151.
Anchukaitis, K.J., D'Arrigo, R.D., Andreu-Hayles, L., Frank, D., Verstege, A., Curtis, A., Buckley, B.M., Jacoby, G.C., Cook, E.R., 2013. Tree-ring-reconstructed summer temperatures from northwestern North America during the last nine centuries. J. Clim. 26, 3001–3012.
Austin, W.E.N., Kroon, D., 1996. Lateglacial sedimentology, foraminifera and stable isotope stratigraphy of the Hebridean Continental Shelf, Northwest Scotland. In: Andrews, J., Austin, W., Bergsten, H., Jennings, A. (Eds.), The Lateglacial Palaeoceanography of the North Atlantic Margins, Geological Society of London, 111, pp. 187–213.
Barber, D.G., Massom, R.A., 2007. The Role of Sea Ice in Arctic and Antarctic Polynyas. In: Elsevier Oceanography Series, 74, pp. 1–54.
Bauch, H., Erlenkeuser, H., Bauch, D., Müller-Lupp, T., Taldenkova, E., 2004. Stable oxygen and carbon isotopes in modern benthic foraminifera from the Laptev Sea shelf: implications for reconstructing proglacial and profluvial environments in the Arctic. Mar. Micropaleontol. 51, 285–300.
Belter, H.J., Krumpen, T., von Albedyll, L., Alekseeva, T.A., Birnbaum, G., Frolov, S.V., Hendricks, S., Herber, A., Polyakov, I., Raphael, I., 2021. Interannual variability in Transpolar Drift summer sea ice thickness and potential impact of Atlantification. Cryosphere 15, 2575–2591.
Bird, B.W., Abbott, M.B., Finney, B.P., Kutchko, B., 2009. A 2000 year varve-based climate record from the Central Brooks Range, Alaska. J. Paleolimnol. 41, 25–41.
Blais, M., Ardyna, M., Gosselin, M., Dumont, D., Bélanger, S., Tremblay, J.-É., Gratton, Y., Marchese, C., Poulin, M., 2017. Contrasting interannual changes in phytoplankton productivity and community structure in the coastal Canadian Arctic Ocean. Limnol. Oceanogr. 62, 2480–2497.
Blott, S., 2010. GRADISTAT ver. 8.0: A Grain Size Distribution and Statistics Package for the Analysis of Unconsolidated Sediments by Sieving or Laser Granulometer. Kenneth Pye Associates, Solihull, UK.
Bringué, M., Rochon, A., 2012. Late Holocene paleoceanography and climate variability over the Mackenzie slope (Beaufort Sea, Canadian Arctic). Mar. Geol. 291, 83–96.
Bronk Ramsey, C., 2008. Deposition models for chronological records. Quat. Sci. Rev. 27, 42–60.
Bronk Ramsey, C., 2009. Bayesian analysis of radiocarbon dates. Radiocarbon 51, 337–360.
Burkovsky, I., 1976. Ecology of Tintinnida (Ciliata) of the White Sea. Zoologicheskii Zhurnal 55, 497–507.
Cage, A.G., Pieńkowski, A.J., Jennings, A., Knudsen, K.L., Seidenkrantz, M.-S., 2021. Comparative analysis of six common foraminiferal species of the genera *Cassidulina*, *Paracassidulina*, and *Islandiella* from the Arctic–North Atlantic domain. J. Micropalaeontol. 40, 37–60.
Carmack, E.C., Macdonald, R.W., 2002. Oceanography of the Canadian Shelf of the Beaufort Sea: a setting for marine life. Arctic 55, 29–45.
Cox, C.J., Stone, R.S., Douglas, D.C., Stanitski, D., Gallagher, M., 2019. The Aleutian Low-Beaufort Sea Anticyclone: a climate index correlated with the timing of springtime melt in the Pacific Arctic cryosphere. Geophys. Res. Lett. 46, 7464–7473.
Cronin, T.M., Gemery, L.J., Briggs, W.M., Brouwers, E.M., Schornikov, E.I., Stepanova, A., Wood, A.M., Yasuhara, M., Siu, S., 2021. NOAA/WDS Paleoclimatology - Arctic Ostracode Database 2020 (AOD2020). [Data Table]. NOAA National Centers for Environmental Information. https://doi.org/10.25921/grn9-9029 (Accessed [2020-11-03).
Cronin, T.M., Gemery, L., Baylee, M.O., Regnier, A.M., Poirier, R., Sienna, S., 2022. Abrupt quaternary ocean-ice events in the Arctic: evidence from the *Ostracod Rabilimis*. Micropaleontology 68, 232–242.
Darby, D.A., Ortiz, J.D., Grosch, C.E., Lund, S.P., 2012. 1,500-year cycle in the Arctic Oscillation identified in Holocene Arctic sea-ice drift. Nat. Geosci. 5, 897–900.
EBA Engineering Consultants Ltd., 1992. Proceedings of the Beaufort Sea Granular Resources Workshop, Part 1: Reports on NOGAP Regional Studies, 11 pp.
Echols, R.J., Fowler, G.A., 1973. Agglutinated tintinnid loricae from some recent and Late Pleistocene shelf sediments. Micropaleontology 19, 431–443.
Ehn, J.K., Reynolds, R.A., Stramski, D., Doxaran, D., Lansard, B., Babin, M., 2019. Patterns of suspended particulate matter across the continental margin in the Canadian Beaufort Sea during summer. Biogeosciences 16, 1583–1605.
Environment Canada, 2020. Historical climate data. Retrieved from http://climate.weather.gc.ca, Accessed [2020-10-12].
Erlenkeuser, H., von Grafenstein, U., 1999. Stable oxygen isotope ratios in benthic carbonate shells of ostracoda, foraminifera, and bivalvia from surface sediments of the Laptev Sea, summer 1993 and 1994. In: Thiede, J., Tomovkhov, L.A. (Eds.), Land-Ocean Systems in the Siberian Arctic. Springer, Berlin, Heidelberg, pp. 503–514.
Falardeau, J., de Vernal, A., Seidenkrantz, M.-S., Cronin, T.M., Gemery, L., Chassiot, L., Fritz, M., Carnero-Bravo, V., Hillaire-Marcel, C., Archambault, P., 2023. Microfaunal recording of recent environmental changes in the Herschel basin, western Arctic Ocean. J. Foraminifer. Res. 53, 20–48. https://doi.org/10.2113/gsjfr.53.1.20.
Fatela, F., Taborda, R., 2002. Confidence limits of species proportions in microfossil assemblages. Mar. Micropaleontol. 45, 169–174.
Fetterer, F., Knowles, K., Meier, W.N., Savoie, M., Windnagel, A.K., 2017. Sea Ice Index, Version 3 [Sea Ice Index Monthly Data with Statistics]. National Snow and Ice Data Center, Boulder, Colorado USA. https://doi.org/10.7265/N5K072F8. Date Accessed 11-23-2022.
Feyling-Hanssen, R.W., Jørgensen, J.A., Knudsen, K.L., Lykke-Andersen, A.-L., 1971. Late Quaternary Foraminifera from Vendsyssel, Denmark and Sandnes, Norway. Bull. Geol. Soc. Den. 21, 67–317.
Frey, K.E., Moore, G., Cooper, L.W., Grebmeier, J.M., 2015. Divergent patterns of recent sea ice cover across the Bering, Chukchi, and Beaufort seas of the Pacific Arctic Region. Prog. Oceanogr. 136, 32–49.
Friesen, T.M., Finkelstein, S.A., Medeiros, A.S., 2020. Climate variability of the Common Era (AD 1–2000) in the eastern North American Arctic: impacts on human migrations. Quat. Int. 549, 142–154.
Fritz, M., Herzschuh, U., Wetterich, S., Lantuit, H., De Pascale, G.P., Pollard, W.H., Schirrmeister, L., 2012. Late glacial and Holocene sedimentation, vegetation, and climate history from easternmost Beringia (northern Yukon Territory, Canada). Quat. Res. 78, 549–560. https://doi.org/10.1016/j.yqres.2012.07.007.
Gemery, L., Cronin, T.M., Briggs, W.M., Brouwers, E.M., Schornikov, E.I., Stepanova, A., Wood, A.M., Yasuhara, M., 2017. An Arctic and Subarctic ostracod database: biogeographic and paleoceanographic applications. Hydrobiologia 786, 59–95.
Gemery, L., Cronin, T.M., Cooper, L.W., Dowsett, H.J., Grebmeier, J.M., 2021. Biogeography and ecology of Ostracoda in the US northern Bering, Chukchi, and Beaufort Seas. PLoS One 16. https://doi.org/10.1371/journal.pone.0251164.
Gemery, L., Cronin, T.M., Cooper, L.W., Roberts, L.R., Keigwin, L.D., Addison, J.A., Leng, M.J., Lin, P., Magen, C., Marot, M.E., Schwartz, V., 2023. Multi-proxy record of ocean-climate variability during the last two millennia on the Mackenzie Shelf, Beaufort Sea. Micropaleontology 69, 345–360. https://doi.org/10.47894/mpal.69.3.04.
Grebmeier, J., Barry, J., 2007. Benthic Processes in Polynyas. In: Elsevier Oceanography Series, 74, pp. 363–390.
Grebmeier, J.M., Cooper, L.W., Feder, H.M., Sirenko, B.I., 2006. Ecosystem dynamics of the Pacific-influenced northern Bering and Chukchi Seas in the Amerasian Arctic. Prog. Oceanogr. 71, 331–361.
Grotheer, H., Meyer, V., Riedel, T., Pfalz, G., Mathieu, L., Hefter, J., Gentz, T., Lantuit, H., Mollenhauer, G., Fritz, M., 2020. Burial and origin of permafrost-derived carbon in the nearshore zone of the southern Canadian Beaufort Sea. Geophys. Res. Lett. 47 https://doi.org/10.1029/2019GL085897.
Guilbault, J.-P., Barrie, J.V., Conway, K., Lapointe, M., Radi, T., 2003. Paleoenvironments of the Strait of Georgia, British Columbia during the last deglaciation: microfaunal and microfloral evidence. Quat. Sci. Rev. 22, 839–857.
Günther, F., Overduin, P.P., Yakshina, I.A., Opel, T., Baranskaya, A.V., Grigoriev, M.N., 2015. Observing Muostakh disappear: permafrost thaw subsidence and erosion of a ground-ice-rich island in response to arctic summer warming and sea ice reduction. Cryosphere 9, 151–178.
Hald, M., Korsun, S., 1997. Distribution of modern benthic foraminifera from fjords of Svalbard, European Arctic. J. Foraminifer. Res. 27, 101–122.
Heaton, T.J., Köhler, P., Butzin, M., Bard, E., Reimer, R.W., Austin, W.E., Ramsey, C.B., Grootes, P.M., Hughen, K.A., Kromer, B., 2020. Marine20—the marine radiocarbon age calibration curve (0–55,000 cal BP). Radiocarbon 62, 779–820.
Husum, K., Hald, M., Stein, R., Weißschnur, M., 2015. Recent benthic foraminifera in the Arctic Ocean and Kara Sea continental margin. Arktos 1, 5.
Hut, G., 1987. Consultants' group meeting on stable isotope reference samples for geochemical and hydrological investigations, IAEA, Vienna 16-18 September 1985 : Report to the Director General, 42 pp.
Jennings, A.E., Helgadóttir, G., 1994. Foraminiferal assemblages from the fjords and shelf of eastern Greenland. J. Foraminifer. Res. 24, 123–144.
Jennings, A., Andrews, J., Reilly, B., Walczak, M., Jakobsson, M., Mix, A., Stoner, J., Nicholls, K.W., Cheseby, M., 2020. Modern foraminiferal assemblages in northern Nares Strait, Petermann Fjord, and beneath Petermann ice tongue, NW Greenland. Arct. Antarct. Alp. Res. 52, 491–511.
Jones, B.M., Arp, C.D., Jorgenson, M.T., Hinkel, K.M., Schmutz, J.A., Flint, P.L., 2009. Increase in the rate and uniformity of coastline erosion in Arctic Alaska. Geophys. Res. Lett. 36 https://doi.org/10.1029/2008GL036205.
Jong, D., Bröder, L., Tanski, G., Fritz, M., Lantuit, H., Tesi, T., Haghipour, N., Eglinton, T. I., Vonk, J.E., 2020. Nearshore zone dynamics determine pathway of organic carbon from eroding permafrost coasts. Geophys. Res. Lett. 47 https://doi.org/10.1029/2020GL088561.
Juhls, B., 2021. Land-Ocean Interactions in Arctic Coastal Waters: Ocean Colour Remote Sensing and Current Carbon Fluxes to the Arctic Ocean. Freie Universität Berlin, 165 pp. https://refubium.fu-berlin.de/handle/fub188/29262.
Khusid, T.A., Korsum, S.A., 1996. Modern benthic foraminiferal assemblages in the Kara Sea. In: Stein, R., et al. (Eds.), Surface-Sediment Composition and Sedimentary Processes in the Central Arctic Ocean and along the Eurasian Continental Margin: Berichte zur Polarforschung 112. Bremerhaven, Alfred Wegener Institute, pp. 96–118.
Kinnard, C., Zdanowicz, C.M., Fisher, D.A., Isaksson, E., de Vernal, A., Thompson, L.G., 2011. Reconstructed changes in Arctic Sea ice over the past 1,450 years. Nature 479, 509–512.
Klein, K.P., Lantuit, H., Heim, B., Fell, F., Doxaran, D., Irrgang, A.M., 2019. Long-term high-resolution sediment and sea surface temperature spatial patterns in Arctic nearshore waters retrieved using 30-year landsat archive imagery. Remote Sens. 11 https://doi.org/10.3390/rs11232791.
Knudsen, K.L., Stabell, B., Seidankrantz, M.S., Eiriksson, J., Blake Jr., W., 2008. Deglacial and Holocene conditions in northernmost Baffin Bay: sediments, foraminifera, diatoms and stable isotopes. Boreas 37, 346–376.

Korsun, S., Hald, M., 2000. Seasonal dynamics of benthic foraminifera in a glacially fed fjord of Svalbard, European Arctic. J. Foraminifer. Res. 30, 251–271.
Kutos, O., Rochon, A., Montero-Serrano, J.C., 2021. Evolution of palaeo-sea-surface conditions and sediment dynamics over the last 2700 years on the Mackenzie Slope, Beaufort Sea (Canadian Arctic). Boreas 50, 893–914.
Kuzyk, Z.Z.A., Gobeil, C., Macdonald, R.W., 2013. ^{210}Pb and ^{137}Cs in margin sediments of the Arctic Ocean: controls on boundary scavenging. Glob. Biogeochem. Cycles 27, 422–439.
Lapointe, F., Francus, P., Lamoureux, S.F., Vuille, M., Jenny, J.-P., Bradley, R.S., Massa, C., 2017. Influence of North Pacific decadal variability on the western Canadian Arctic over the past 700 years. Clim. Past 13, 411–420.
Lin, P., Pickart, R.S., Fissel, D., Ross, E., Kasper, J., Bahr, F., Torres, D.J., O'Brien, J., Borg, K., Melling, H., 2020. Circulation in the vicinity of Mackenzie Canyon from a year-long mooring array. Prog. Oceanogr. 187 https://doi.org/10.1016/j.pocean.2020.102396.
Luoto, T.P., Nevalainen, L., Kubischta, F., Kultti, S., Knudsen, K.L., Salonen, V.P., 2011. Late quaternary ecological turnover in high arctic Lake Einstaken, Nordaustlandet, Svalbard (80 N). Geografiska Annaler: Series A, Physical Geography 93, 337–354.
MacDonald, G.M., Case, R.A., 2005. Variations in the Pacific Decadal Oscillation over the past millennium. Geophys. Res. Lett. 32 https://doi.org/10.1029/2005GL022478.
Mackensen, A., 2008. On the use of benthic foraminiferal δ^{13}C in palaeoceanography: constraints from primary proxy relationships. Geol. Soc. Lond., Spec. Publ. 303, 121–133.
Madsen, H.B., Knudsen, K.L., 1994. Recent foraminifera in shelf sediments of the Scoresby Sund fjord, East Greenland. Boreas 23, 495–504.
Mäkelä, A., Witte, U., Archambault, P., 2018. Short-term processing of ice algal-and phytoplankton-derived carbon by Arctic benthic communities revealed through isotope labelling experiments. Mar. Ecol. Prog. Ser. 600, 21–39.
Mann, M.E., Zhang, Z., Rutherford, S., Bradley, R.S., Hughes, M.K., Shindell, D., Ammann, C., Faluvegi, G., Ni, F., 2009. Global signatures and dynamical origins of the Little Ice Age and Medieval Climate Anomaly. Science 326, 1256–1260.
Mantua, N.J., Hare, S.R., 2002. The Pacific decadal oscillation. J. Oceanogr. 58, 35–44.
McCorkle, D.C., Keigwin, L.D., Corliss, B.H., Emerson, S.R., 1990. The influence of microhabitats on the carbon isotopic composition of deep-sea benthic foraminifera. Paleoceanography 5, 161–185.
McDougall, K.A., Brouwers, E.M., Smith, P., 1986. Micropaleontology and sedimentology of the PB borehole series, Prudhoe Bay, Alaska. U.S. Geol. Surv. Bull. 1598 https://doi.org/10.3133/b1598, 62 pp.
McNeely, R., Dyke, A., Southon, J., 2006. Canadian marine reservoir ages: preliminary data assessment. Geological Survey of Canada (Open File 5049). 3 pp.
Meunier, A., 1919. Mikroplankton de la mer Flamande. III. Les Péridiniens: Mémoires du Musée Royal d'Histoire Naturelle de Belgique 8, 1–116.
Meyer, H., Schönicke, L., Wand, U., Hubberten, H.W., Friedrichsen, H., 2000. Isotope studies of hydrogen and oxygen in ground-ice experiences with the equilibration technique. Environ. Health Stud. 36, 133–149. https://doi.org/10.1080/10256010008032939.
Mioduszewski, J., Vavrus, S., Wang, M., 2018. Diminishing Arctic Sea ice promotes stronger surface winds. J. Clim. 31, 8101–8119.
Mulligan, R.P., Perrie, W., 2019. Circulation and structure of the Mackenzie River plume in the coastal Arctic Ocean. Cont. Shelf Res. 177, 59–68.
Mulligan, R.P., Perrie, W., Solomon, S., 2010. Dynamics of the Mackenzie River plume on the inner Beaufort shelf during an open water period in summer. Estuar. Coast. Shelf Sci. 89, 214–220.
Murray, J.W., 1991. Ecology and Palaeoecology of Benthic Foraminifera. Longman, Harlow, p. 397.
Murray, J.W., 2006. Ecology and Applications of Benthic Foraminifera. Cambridge University Press, 440 pp.
Nadaï, G., Nöthig, E.-M., Fortier, L., Lalande, C., 2021. Early snowmelt and sea ice breakup enhance algal export in the Beaufort Sea. Prog. Oceanogr. 190 https://doi.org/10.1016/j.pocean.2020.102479.
Nardelli, M.P., Fossile, E., Péron, O., Howa, H., Mojtahid, M., 2023. Early taphonomy of benthic Foraminifera in Storfjorden 'sea-ice factory': the agglutinated/calcareous ratio as a proxy for brine persistence. Boreas 52, 109–123. https://doi.org/10.1111/bor.12592. ISSN 0300-9483.
Nicolle, M., Debret, M., Massei, N., Colin, C., de Vernal, A., Divine, D., Werner, J.P., Hormes, A., Korhola, A., Linderholm, H.W., 2018. Climate variability in the subarctic area for the last 2 millennia. Clim. Past 14, 101–116.
Notz, D., Stroeve, J., 2016. Observed Arctic Sea-ice loss directly follows anthropogenic CO2 emission. Science 354, 747–750.
Obu, J., Lantuit, H., Fritz, M., Pollard, W.H., Sachs, T., Günther, F., 2016. Relation between planimetric and volumetric measurements of permafrost coast erosion: a case study from Herschel Island, western Canadian Arctic. Polar Res. 35 https://doi.org/10.3402/polar.v35.30313.
Oksanen, J., Blanchet, F.G., Kindt, R., Legendre, P., Minchin, P.R., O'hara, R., Simpson, G.L., Solymos, P., Stevens, M.H.H., Wagner, H., 2013. Package 'vegan'. Community ecology package, version 2, pp. 1–295.
Olausson, E., 1982. The Pleistocene/Holocene boundary in South-Western Sweden: Sveriges Geologiska Undersökning. Ser. C, 794, 288 p.
Overeem, I., Anderson, R.S., Wobus, C.W., Clow, G.D., Urban, F.E., Matell, N., 2011. Sea ice loss enhances wave action at the Arctic coast. Geophys. Res. Lett. 38 https://doi.org/10.1029/2011GL048681.
Paranjape, M.A., 1987. The seasonal cycles and vertical distribution of tintinnines in Bedford Basin, Nova Scotia, Canada. Can. J. Zool. 65, 41–48.
Patterson, R.T., Guilbault, J.-P., Thomson, R.E., 2000. Oxygen level control on foraminiferal distribution in Effingham Inlet, Vancouver Island, British Columbia, Canada. J. Foraminifer. Res. 30, 321–335.
Pearce, C., Varhelyi, A., Wastegård, S., Muschitiello, F., Barrientos, N., O'Regan, M., Cronin, T.M., Gemery, L., Semiletov, I., Backman, J., 2017. The 3.6 ka Aniakchak tephra in the Arctic Ocean: a constraint on the Holocene radiocarbon reservoir age in the Chukchi Sea. Clim. Past 13, 303–316.
Pfalz, G., 2017. Lateral transport of sediment and organic matter, derived from coastal erosion, into the nearshore zone of the southern Beaufort Sea, Canada. Technische Universität Dresden, 86 pp. https://epic.awi.de/id/eprint/44364/.
Pickart, R.S., 2004. Shelfbreak circulation in the Alaskan Beaufort Sea: mean structure and variability. J. Geophys. Res. Oceans 109. https://doi.org/10.1029/2003JC001912.
Pickart, R.S., Spall, M.A., Moore, G.W., Weingartner, T.J., Woodgate, R.A., Aagaard, K., Shimada, K., 2011. Upwelling in the Alaskan Beaufort Sea: Atmospheric forcing and local versus non-local response. Prog. Oceanogr. 88, 78–100.
Pickart, R.S., Spall, M.A., Mathis, J.T., 2013. Dynamics of upwelling in the Alaskan Beaufort Sea and associated shelf–basin fluxes. Deep-Sea Res. I Oceanogr. Res. Pap. 76, 35–51.
Polyak, L., Korsun, S., Febo, L.A., Stanovoy, V., Khusid, T., Hald, M., Paulsen, B.E., Lubinski, D.J., 2002. Benthic foraminiferal assemblages from the southern Kara Sea, a river-influenced Arctic marine environment. J. Foraminifer. Res. 32, 252–273.
Polyak, L., Stanovoy, V., Lubinski, D.J., 2003. Stable isotopes in benthic foraminiferal calcite from a river-influenced Arctic marine environment, Kara and Pechora Seas. Paleoceanography 18. https://doi.org/10.1029/2001PA000752.
Porter, T.J., Pisaric, M.F., Kokelj, S.V., 2013. A ring-width-based reconstruction of June–July minimum temperatures since AD 1245 from white spruce stands in the Mackenzie Delta region, northwestern Canada. Quat. Res. 80, 167–179.
R Core Team, 2021. R: A Language and Environment for Statistical Computing. R Foundation for Statistical Computing, Vienna, Austria. https://www.R-project.org/.
Radosavljevic, B., Lantuit, H., Pollard, W., Overduin, P., Couture, N., Sachs, T., Helm, V., Fritz, M., 2016. Erosion and flooding—threats to coastal infrastructure in the Arctic: a case study from Herschel Island, Yukon Territory, Canada. Estuar. Coasts 39, 900–915.
Rainville, L., Woodgate, R.A., 2009. Observations of internal wave generation in the seasonally ice-free Arctic. Geophys. Res. Lett. 36 https://doi.org/10.1029/2009GL041291.
Richerol, T., Rochon, A., Blasco, S., Scott, D.B., Schell, T.M., Bennett, R.J., 2008. Evolution of paleo sea-surface conditions over the last 600 years in the Mackenzie Trough, Beaufort Sea (Canada). Mar. Micropaleontol. 68, 6–20.
Rigor, I.G., Wallace, J.M., Colony, R.L., 2002. Response of sea ice to the Arctic Oscillation. J. Clim. 15, 2648–2663.
Rogers, G., Roff, J., Lynn, D., 1981. Tintinnids of Chesterfield Inlet, Northwest Territories. Can. J. Zool. 59, 2360–2364.
Rühland, K., Priesnitz, A., Smol, J.P., 2003. Paleolimnological evidence from diatoms for recent environmental changes in 50 lakes across Canadian Arctic treeline. Arct. Antarct. Alp. Res. 35, 110–123.
Rytter, F., Knudsen, K.L., Seidenkrantz, M.-S., Eiríksson, J., 2002. Modern distribution of benthic foraminifera on the North Icelandic shelf and slope. J. Foraminifer. Res. 32, 217–244.
Sanchez-Cabeza, J., Ruiz-Fernández, A., 2012. ^{210}Pb sediment radiochronology: an integrated formulation and classification of dating models. Geochimica et Cosmochimica Acta 82, 183–200.
Schell, T.M., Scott, D.B., Rochon, A., Blasco, S., 2008. Late Quaternary paleoceanography and paleo-sea ice conditions in the Mackenzie Trough and Canyon, Beaufort Sea. Can. J. Earth Sci. 45, 1399–1415.
Schlitzer, R., 2018. Ocean Data View, Alfred Wegener Institute. https://odv.awi.de.
Schulze, L.M., Pickart, R.S., 2012. Seasonal variation of upwelling in the Alaskan Beaufort Sea: Impact of sea ice cover. J. Geophys. Res. Oceans 117. https://doi.org/10.1029/2012JC007985.
Scott, D.B., Schell, T., Rochon, A., Blasco, S., 2008a. Modern benthic foraminifera in the surface sediments of the Beaufort Shelf, Slope and Mackenzie Trough, Beaufort Sea, Canada: taxonomy and summary of surficial distributions. J. Foraminifer. Res. 38, 228–250.
Scott, D.B., Schell, T., Rochon, A., Blasco, S., 2008b. Benthic foraminifera in the surface sediments of the Beaufort Shelf and slope, Beaufort Sea, Canada: applications and implications for past sea-ice conditions. J. Mar. Syst. 74, 840–863.
Scott, D.B., Schell, T., St-Onge, G., Rochon, A., Blasco, S., 2009. Foraminiferal assemblage changes over the last 15,000 years on the Mackenzie-Beaufort Sea Slope and Amundsen Gulf, Canada: Implications for past sea ice conditions. Paleoceanography 24. https://doi.org/10.1029/2007PA001575.
Screen, J.A., Francis, J.A., 2016. Contribution of sea-ice loss to Arctic amplification is regulated by Pacific Ocean decadal variability. Nat. Clim. Chang. 6, 856–860.
Seidenkrantz, M.-S., 2013. Benthic foraminifera as palaeo sea-ice indicators in the subarctic realm–examples from the Labrador Sea–Baffin Bay region. Quat. Sci. Rev. 79, 135–144.
Seidenkrantz, M.-S., Kuijpers, A., Aagaard-Sørensen, S., Lindgreen, H., Olsen, J., Pearce, C., 2021. Evidence for influx of Atlantic water masses to the Labrador Sea during the last Glacial Maximum. Sci. Rep. 11, 1–14.
Seidenstein, J.L., Cronin, T.M., Gemery, L., Keigwin, L.D., Pearce, C., Jakobsson, M., Coxall, H.K., Wei, E.A., Driscoll, N.W., 2018. Late Holocene paleoceanography in the Chukchi and Beaufort Seas, Arctic Ocean, based on benthic foraminifera and ostracods. Arktos 4. https://doi.org/10.1007/s41063-018-0058-7.
Shackleton, N., 1974. Attainment of isotopic equilibrium between ocean water and the benthonic foraminifera genus *Uvigerina*: isotopic changes in the ocean during the last glacial. Colloques Internationaux du C.N.R.S. 219, 203–209.
Shannon, C.E., 1948. A mathematical theory of communication. Bell Syst. Tech. J. 27, 379–423.

Souto, S., 1973. Contribución al conocimiento de los tintínnidos de agua dulce de la República Argentina. I Río de la Plata y Delta del Paraná. Physis 32, 249–254.
Spreen, G., Kwok, R., Menemenlis, D., 2011. Trends in Arctic sea ice drift and role of wind forcing: 1992–2009. Geophys. Res. Lett. 38 https://doi.org/10.1029/2011GL048970.
Stepanova, A., Taldenkova, E., Bauch, H.A., 2003. Recent Ostracoda from the Laptev Sea (Arctic Siberia): species assemblages and some environmental relationships. Mar. Micropaleontol. 48, 23–48.
Stepanova, A., Taldenkova, E., Simstich, J., Bauch, H.A., 2007. Comparison study of the modern ostracod associations in the Kara and Laptev seas: ecological aspects. Mar. Micropaleontol. 63, 111–142.
Stepanova, A., Obrochta, S., Quintana Krupinski, N.B., Hyttinen, O., Kotilainen, A., Andrén, T., 2019. Late Weichselian to Holocene history of the Baltic Sea as reflected in ostracod assemblages. Boreas 48, 761–778.
Stuiver, M., Reimer, P.J., 1993. Extended ^{14}C data base and revised CALIB 3.0 ^{14}C age calibration program. Radiocarbon 35, 215–230.
Thompson, D.W., Wallace, J.M., 1998. The Arctic Oscillation signature in the wintertime geopotential height and temperature fields. Geophys. Res. Lett. 25, 1297–1300.
Tian, S.Y., Yasuhara, M., Hong, Y., Huang, H.-H.M., Iwatani, H., Chiu, W.-T.R., Mamo, B., Okahashi, H., Rasmussen, T.L., 2020. Deglacial–Holocene Svalbard paleoceanography and evidence of meltwater pulse 1B. Quat. Sci. Rev. 233 https://doi.org/10.1016/j.quascirev.2020.106237.
Tremblay, J.-É., Bélanger, S., Barber, D., Asplin, M., Martin, J., Darnis, G., Fortier, L., Gratton, Y., Link, H., Archambault, P., 2011. Climate forcing multiplies biological productivity in the coastal Arctic Ocean. Geophys. Res. Lett. 38 https://doi.org/10.1029/2011GL048825.
Tremblay, J.-É., Robert, D., Varela, D.E., Lovejoy, C., Darnis, G., Nelson, R.J., Sastri, A.R., 2012. Current state and trends in Canadian Arctic marine ecosystems: I. Primary production. Clim. Chang. 115, 161–178.
Ullrich, A.D., Cowan, E.A., Zellers, S.D., Jaeger, J.M., Powell, R.D., 2009. Intra-annual variability in benthic foraminiferal abundance in sediments of Disenchantment Bay, an Alaskan glacial fjord. Arct. Antarct. Alp. Res. 41, 257–271.
Usher, P.J., 2002. Inuvialuit use of the Beaufort Sea and its resources, 1960-2000. Arctic 18–28.
Viau, A.E., Gajewski, K., 2009. Reconstructing millennial-scale, regional paleoclimates of boreal Canada during the Holocene. J. Clim. 22, 316–330.
Voltski, I., Korsun, S., Pillet, L., Pawlowski, J., 2015. *Protoelphidium niveum* and the taxonomy of "lower" elphidiids. J. Foraminifer. Res. 45, 250–263.
West, G., Nilsson, A., Geels, A., Jakobsson, M., Moros, M., Muschitiello, F., Pearce, C., Snowball, I., O'Regan, M., 2022. Late Holocene Paleomagnetic Secular Variation in the Chukchi Sea, Arctic Ocean. Geochem. Geophys. Geosyst. 23 https://doi.org/10.1029/2021GC010187.
Williams, B., Carmack, E., 2012. Ocean water and sea ice. In: Burn, C.R. (Ed.), Herschel Island Qikiqtaryuk: A Natural and Cultural History of Yukon's Arctic Island. University of Calgary Press, Calgary, pp. 54–59.
Wollenburg, J.E., Kuhnt, W., 2000. The response of benthic foraminifera to carbon flux and primary production in the Arctic Ocean. Mar. Micropaleontol. 40, 189–231.
Wollenburg, J.E., Mackensen, A., 1998. Living benthic foraminifera from the central Arctic Ocean: faunal composition, standing stock and diversity. Mar. Micropaleontol. 34, 153–185.
Wolter, J., Lantuit, H., Herzschuh, U., Stettner, S., Fritz, M., 2017. Tundra vegetation stability versus lake-basin variability on the Yukon Coastal Plain (NW Canada) during the past three centuries. The Holocene 27, 1846–1858.
Wood, K.R., Bond, N.A., Danielson, S.L., Overland, J.E., Salo, S.A., Stabeno, P.J., Whitefield, J., 2015. A decade of environmental change in the Pacific Arctic region. Prog. Oceanogr. 136, 12–31.
Zhang, M., Perrie, W., Long, Z., 2019. Springtime North Pacific Oscillation and summer sea ice in the Beaufort Sea. Clim. Dyn. 53, 671–686.